NEUROSCIENCE

# Instant noninvasive near-infrared deep brain stimulation using optoelectronic nanoparticles without genetic modification

**Shuang Jin[1], Jiazhi Li[1], Luyue Jiang[1], Yifei Ye[1], Chenguang Ma[1], Yingkang Yang[1,2], Haoyang Su[1,2], Lusha Gao[1], Min Ni[3], Yiping Zhao[1,2], Ye Tian[1,2], Gen Li[1,2], Jinwei Shi[3], Kaihuan Zhang[1,2,4], Pengyi Tang[1,2,5], Yu Yuan[6], Bin Lai[6], Ming Chen[6], Liuyang Sun[1,2,4]***



**Noninvasive transcranial neuromodulation of deep brain regions is a longstanding goal in neuroscience. While optogenetics enables remote neural control, it is constrained by shallow tissue penetration of visible light and delayed onset due to required opsin expression. Here, we introduce a neuromodulation technique using hybrid upconversion and photovoltaic (HUP) nanoparticles, which eliminates the need for genetic modification and affords near-infrared (NIR) activation of neurons in wild-type mice. This method converts deeply penetrating NIR light into localized electrical stimuli, enabling immediate and precise modulation in deep brain. In vitro patch-clamp experiments confirm neuronal activation upon HUP application. In vivo, we achieve remote NIR neuromodulation in the medial septum and ventral tegmental area 7 days postinjection, effectively modulating neuronal activity, suppressing seizures, and triggering dopamine release. This minimally invasive approach offers a versatile tool kit for investigating neural processes in mammals, with potential applications across diverse brain regions through customizable nanoparticle engineering.**

## INTRODUCTION

Precise neuromodulation is essential for exploring neural mechanisms and improving treatments for neurological disorders (*1*, *2*). While conventional electrical implants provide effective stimulation (*3*–*5*), their invasiveness often leads to tissue damage, infection, and scarring, creating a demand for less invasive alternatives. Optical stimulation has emerged as a promising solution in animal models (*6*, *7*), affording high spatiotemporal resolution and the ability to target specific neuron subtypes. Among these methods, optogenetics has been revolutionary, which uses light to control neural activities through light-sensitive microbial opsins expressed in specific neurons. However, optogenetics faces two major challenges: (i) the use of visible light, which is scattered and absorbed strongly in biological tissues, necessitating implanted optical fibers for deep-brain stimulation, causing the same tissue damage seen with electrical implants (*8*, *9*), and (ii) the intrinsic need for genetic modification (*10*–*12*), which introduces delays of several weeks post–viral delivery for full opsin expression and limits clinical translation.

To address these limitations, researchers have explored solutions in two key areas. First, to overcome light penetration challenges, recent approaches include the development of red-shifted opsins responsive to longer wavelengths (*13*), the use of upconversion nanoparticles (UCNPs) that convert near-infrared (NIR) light into shorter wavelengths (*10*, *14*–*17*), and thermogenetics involving heat-sensitive ion channels (*18*–*22*). However, these techniques still rely on genetic modification and complex molecular designs (*23*, *24*), limiting their immediacy and broader applicability across neuron populations. Second, efforts to bypass genetic modification have led to nongenetic optical neuromodulation techniques, which use transducers to convert light into acoustic (*25*–*27*), mechanical (*28*, *29*), or electrical stimuli (*30*–*37*), modulating neural activity without the need for opsins. For instance, various organic and inorganic photovoltaic materials have been used to convert visible light into photocurrents for direct stimulation of biological tissues in vivo. Notably, silicon (*38*–*42*), metal oxides (*43*, *44*), and organic electrolytic photocapacitors (*45*–*47*) have demonstrated the ability to transform ultraviolet (UV) and visible light into electrical stimuli, which have been applied to the retina, heart, and peripheral nerves. However, these methods are primarily restricted to superficial applications because of the limited penetration depth of visible light. Therefore, there remains a critical unmet need for a method that enables immediate, noninvasive, and remote deep brain stimulation in wild-type animals without genetic modification.

In this work, we developed an instant NIR deep brain stimulation method using readily accessible hybrid-UCNP and photovoltaic (HUP) materials in living mice, eliminating the need for genetic modification and the associated waiting period. This combination was chosen on the basis of two main considerations. First, the deep tissue penetration of NIR light is captured and converted into blue light by rare earth–based UCNP. Second, the blue light is then transformed into localized electrical stimuli by photovoltaic materials—specifically, $WO_{3-x}$ (*48*, *49*) in this proof-of-concept study—enabling precise neural activation in nongenetically modified animals. Unlike optogenetics, which requires weeks for opsin expression, the photovoltaic method provides immediate neural activation upon NIR excitation postinjection. By combining the strengths of both key components, we demonstrate that hybrid optoelectronic nanoparticles can efficiently achieve noninvasive NIR neurostimulation.

[1]2020 X-Lab, Shanghai Institute of Microsystem and Information Technology, Chinese Academy of Sciences, Shanghai 200050, China. [2]School of Integrated Circuits, University of Chinese Academy of Sciences, Beijing 100049, China. [3]Applied Optics Beijing Area Major Laboratory and Key Laboratory of Multiscale Spin Physics of Ministry of Education, School of Physics and Astronomy, Beijing Normal University, Beijing 100875, China. [4]State Key Laboratory of Transducer Technology, Shanghai Institute of Microsystem and Information Technology, Chinese Academy of Sciences, Shanghai 200050, China. [5]National Key Laboratory of Materials for Integrated Circuits, Shanghai Institute of Microsystem and Information Technology, Chinese Academy of Sciences, Shanghai 200050, China. [6]State Key Laboratory of Medical Neurobiology, MOE Frontier Center for Brain Science, Department of Neurology of Zhongshan Hospital, School of Basic Medical Sciences, Institutes of Brain Science, Fudan University, Shanghai 200032, China.
*Corresponding author. Email: liuyang.sun@mail.sim.ac.cn

Our in vitro patch clamp experiments demonstrated that neurons in brain slices responded with action potentials immediately after HUP was applied and NIR stimulation at 980 nm was delivered. For in vivo validation, we successfully stimulated neurons in deep brain regions, including the medial septum (MS) and ventral tegmental area (VTA). Transcranial NIR stimulation of the MS region injected with HUP led to notable hippocampal electrophysiological responses, suppressing seizure activity and inducing synchronous electrical signals as early as 7 days postinjection. In the VTA, NIR stimulation effectively activated dopamine neurons, confirmed by real-time electrochemical measurements as early as 7 days postinjection. Behavioral observations further showed that NIR stimulation in the VTA induced spatial location preference in a Y-maze, providing functional evidence of neural modulation. Immunofluorescence histology also confirmed substantial c-Fos expression in brain regions near the injected HUP, indicating effective cellular activation. Our approach represents a major step forward in the development of faster-acting, less invasive, and more versatile neuromodulation techniques, positioning it as an important advancement in the field of noninvasive neural stimulation.

## RESULTS

### Design principle and optoelectronic performance of HUP

We hypothesized that HUP-mediated NIR irradiation could effectively stimulate deep brain neurons in wild-type rodents as illustrated in Fig. 1A. This assumption is based on the efficiency of NIR upconversion by the nanoparticles (*15*), the energy transfer from UCNPs to $WO_{3-x}$, and the photocurrent conversion efficiency of $WO_{3-x}$. Specifically, we selected rare-earth elements for doping UCNPs because of their proven efficiency in facilitating upconversion processes (*50*), which are essential for converting NIR light to the visible spectrum as illustrated in Fig. 1B. $WO_{3-x}$ was chosen for its bandgap properties, enabling efficient absorption of the blue light emitted by UCNPs (*51*), which is critical for photocurrent generation as illustrated in Fig. 1C. Furthermore, both nanoparticles demonstrated good biocompatibility (*3*, *52*), evidenced by minimal glial fibrillary acidic protein–positive ($GFAP^+$) astrocyte and $Iba\text{-}1^+$ microglial activation 3 weeks postinjection of HUP in comparison to phosphate-buffered saline (PBS) as shown in fig. S1.

Initially, we engineered UCNPs with an absorption peak at 980 nm, matching the biological tissue optical window to maximize tissue penetration and configured them to emit blue light, which is efficiently absorbed by $WO_{3-x}$. We synthesized blue-emitting $NaYF_4$:Yb/Tm nanocrystals coated with an optically inert $NaYF_4$ shell to prevent luminescence quenching by solvent molecules and further decorated these nanocrystals with silica to enhance biocompatibility. These core-shell UCNPs, with an average diameter of 49 nm as confirmed by transmission electron microscopy (TEM) (Fig. 2A and fig. S2), exhibit optimized absorbance at 980 nm (Fig. 2D). The microstructure of the UCNP was confirmed by its x-ray diffraction (XRD) pattern as shown in fig. S3. Their photoluminescence measurements display a characteristic upconversion emission spectrum with main emission peak at 450 nm upon 980-nm excitation (Fig. 2E), achieving a conversion yield of approximately 1.4% (Fig. 2F). This upconverted photon energy surpasses the bandgap of $WO_{3-x}$, ensuring efficient absorption.

$WO_{3-x}$ plays a pivotal role in converting the blue light into a photocurrent that can directly stimulate wild-type neurons. We synthesized $WO_{3-x}$ nanorods via a hydrothermal process, resulting in rods ranging from 20 to 100 nm in length and about 10 nm in diameter (Fig. 2B). The phase of $WO_{3-x}$ is confirmed by XRD pattern in fig. S4. We note that pristine $WO_3$ exhibits weak absorption around 450 ~ 500 nm due to its bandgap. To enhance absorption at 450 nm, we introduced oxygen defects to form $WO_{3-x}$, creating sub-band states that improve efficiency and store photogenerated electrons, following prior studies (*48*). The $WO_{3-x}$ bandgap is ~2.47 eV (fig. S5), but these defects enable effective absorption of the 450-nm blue emission from UCNPs, as confirmed by photocurrent measurements (fig. S6A). Voltage-clamp recordings further demonstrate that $WO_{3-x}$ converts blue light into electrical signals, activating neurons in all 11 trials across two neurons under 470-nm illumination (fig. S6B).

In addition, the proximity of UCNPs and $WO_{3-x}$ (Fig. 2C) facilitates efficient absorption via far-field radiative or near-field nonradiative energy transfer (*53*–*55*), minimizing dispersion and maximizing the photovoltaic effect. Specifically, energy transfer depends on their relative distance: In the far-field regime (separations much larger

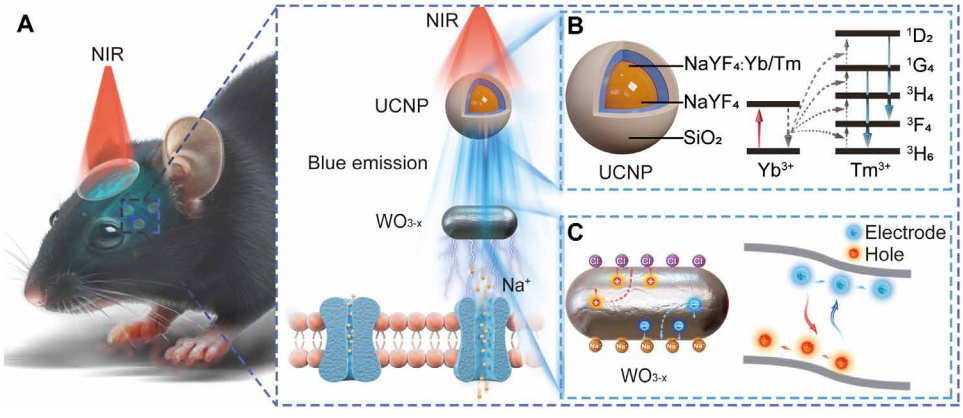


**Fig. 1. Schematic illustration of HUP-mediated NIR optoelectronics for deep brain stimulation.** (**A**) Schematic illustration of all-optical, non-optogenetic deep brain stimulation enabled by an HUP system. (**B**) Design schematic of a blue-emitting $NaYF_4$:Yb/Tm@$NaYF_4$@$SiO_2$ particle, where the band structure of rare earth elements facilitates the upconversion of NIR light. (**C**) Under blue light excitation, electrons and holes in $WO_{3-x}$ generate an internal electric field resulting in direct electric stimuli to nearby neurons.

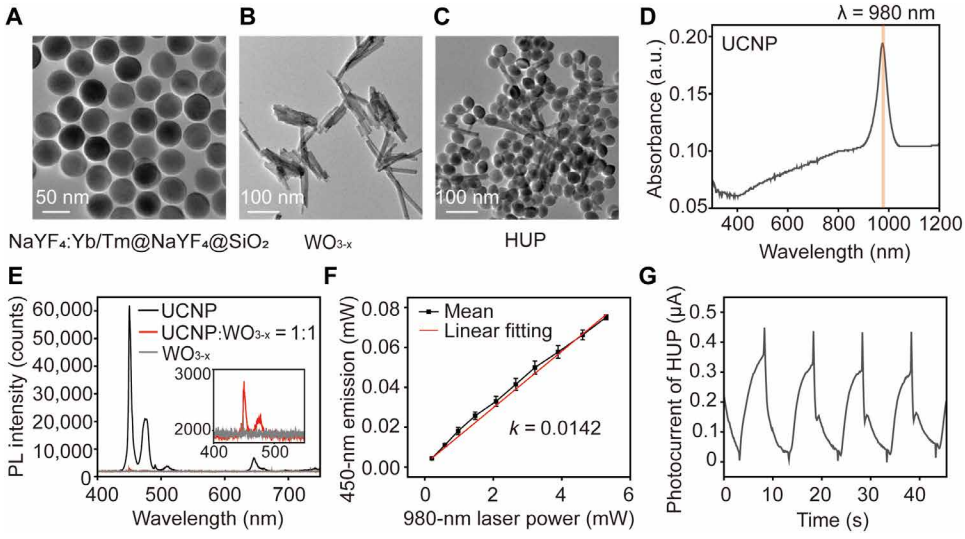


**Fig. 2. HUP-mediated NIR optoelectronics.** (**A**) TEM image showing silica-coated UCNPs. (**B**) TEM image showing $WO_{3-x}$ nanorods. (**C**) TEM image showing the HUP mixture. (**D**) Absorption spectrum of UCNPs, optimized to show an absorbance peak at 980 nm. (**E**) Photoluminescence spectra of UCNPs, HUP, and $WO_{3-x}$ individually. When the UCNPs and $WO_{3-x}$ mass ratio is 1:1, the blue emission intensity drops by 95% compared to pure UCNPs. (**F**) Upconversion emission intensity upon 980-nm excitation at various laser powers. The upconversion efficiency is calculated around 1.4%. (**G**) Photocurrent of HUP recorded in Amperometric i-t mode under 1.2 W CW NIR irradiation (26 W/cm$^2$). a.u., arbitrary units.

than the ~450-nm wavelength), radiative transfer occurs as blue light emitted by UCNPs is absorbed by $WO_{3-x}$, while at nanometer-scale separations, near-field nonradiative transfer dominates via dipole-dipole interactions akin to Förster resonance energy transfer, enabling efficient energy transfer without photon emission. The random distribution and close proximity of UCNPs and $WO_{3-x}$ nanorods (Fig. 2C) suggest that both mechanisms contribute, as evidenced by a 95% reduction in the 450-nm photoluminescence peak at equal UCNP: $WO_{3-x}$ mass concentrations (Fig. 2E and fig. S7). We selected this equal mass ratio for subsequent experiments.

Further, we assessed the photocurrent generated by HUP upon excitation at 980 nm. These quantitative measurements—considering the upconversion efficiency, blue light absorption, $WO_{3-x}$ incident photon-to-current efficiency (*56*), and the 980-nm light scattering rate in brain tissue—suggested that delivering approximately 1 W of 980-nm laser light above the mouse skull through an optic fiber could achieve an effective current density of about hundreds of microampere per square centimeter in the brain, sufficient for neuronal activation (see the Supplementary Materials for details). Confirmatory tests with HUP on a fluorine tin oxide (FTO)–coated glass substrate at 0-V bias voltage, excited by a 1-W 980-nm laser of ~1 mm$^2$, produced a current ~0.5 μA (Fig. 2G). Considering that the FTO is about 15 mm beneath the PBS, while the deep brain we are interested in is only about 4 mm beneath the skull, the photocurrent generated in the deep brain is expected to be tens to hundreds of microampere, well above the neuronal activation threshold as we would explore in the later in vivo tests. We note that under NIR illumination, the HUP system generates electron-hole pairs, a fundamental process for converting photonic energy into an electrical field. Since the photovoltaic effect can be classified as either capacitive or Faradaic, it is crucial to clarify that the HUP mechanism follows a capacitive process, as confirmed by the absence of redox peaks in our cyclic voltammetry at 0 V bias (fig. S8). This capacitive charge separation and storage at the solid-liquid interface drives local ionic currents in the extracellular space, enabling neuromodulation without oxidation or reduction reactions. Therefore, throughout the above measurements and calculations, HUP have demonstrated the ability to efficiently convert NIR to blue light via UCNPs, with subsequent efficient photocurrent generation by $WO_{3-x}$, underscoring its potential for the application in noninvasive neural modulation.

## In vitro electrophysiological validation of HUP in neuronal activation

Our initial investigations began with an in vitro experiment to elucidate the foundational mechanisms of HUP-mediated neuromodulation (Fig. 3A). We injected trace amounts of HUP (Fig. 3B), UCNPs, or $WO_{3-x}$ solution into brain tissue slices from the VTA region, respectively. Following the injection, immediate photocurrents were observed in voltage-clamp mode using patch clamp techniques when NIR stimulation at 980 nm, delivered via an optical fiber, was applied to brain slices containing HUP (Fig. 3C). This response was synchronized with the 200-ms NIR pulses at 0.5 Hz, indicating a direct correlation between NIR exposure and electrical activity in the neurons (Fig. 3D). In the absence of HUP, no photocurrents were detected, underscoring the specificity of our HUP system (Fig. 3C).

Further assessments in current-clamp mode showed pronounced membrane depolarization, sufficient to evoke spikes in neurons proximal to the HUP. Whole-cell electrophysiological recordings confirmed the excitation effect of HUP in VTA and MS neurons (Fig. 3, E and F). In addition to the representative recordings shown in Fig. 3, data from another 11 neurons in the VTA slices under various irradiation conditions are provided in fig. S9. Across these recordings, we consistently observed robust neuronal responses, either as subthreshold depolarizations or action potentials with few exceptions from experimental group, demonstrating the high effectiveness of HUP-mediated NIR stimulation.

While this study primarily focuses on deep brain regions, the HUP methodology is applicable to other brain areas as well. To further

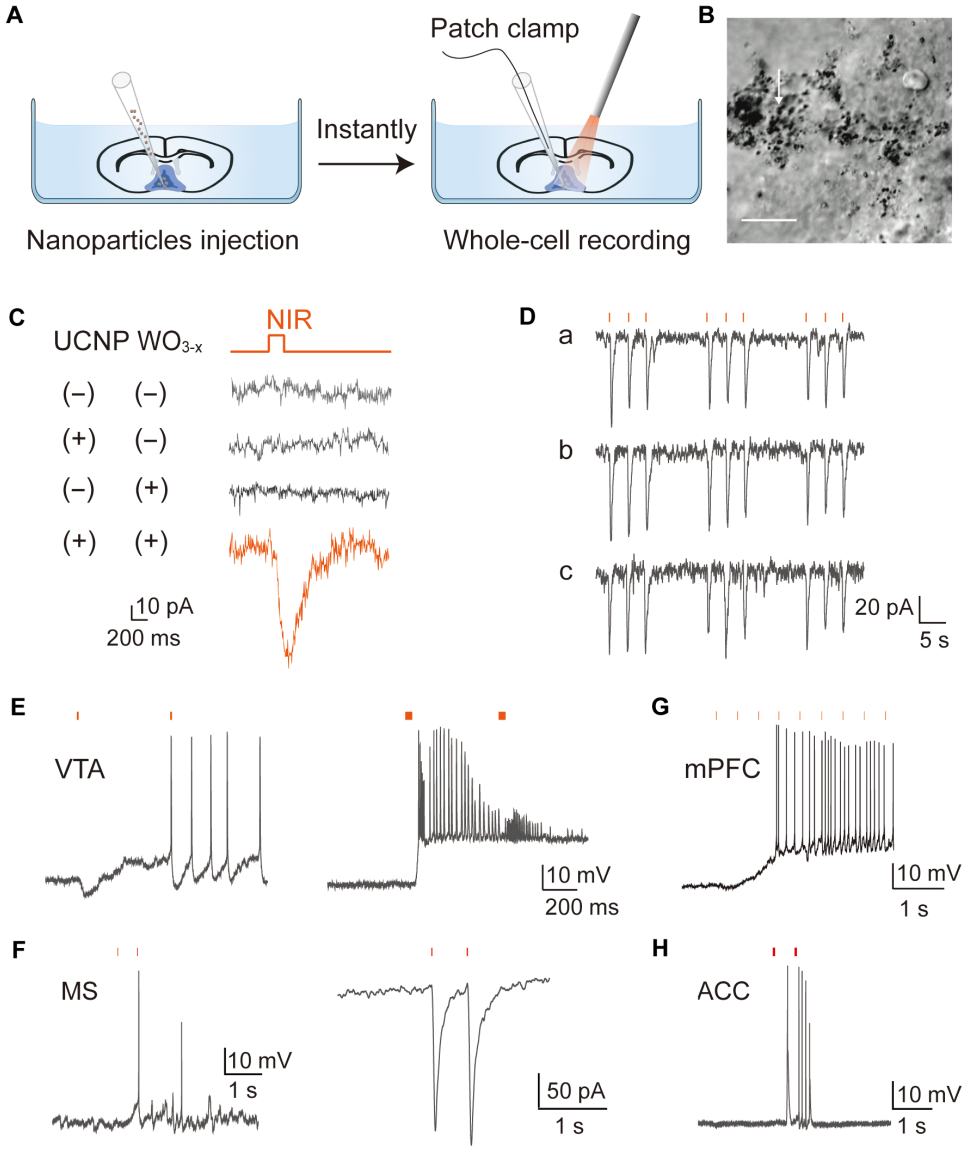


**Fig. 3. Validation of HUP excitation in vitro.** (**A**) Experimental scheme. Coronal acute slices containing the VTA, MS, mPFC, or ACC were prepared, and in vitro whole-cell recordings were performed. (**B**) Representative image of HUP into brain tissue slices from the VTA. Scale bars, 100 μm. (**C** and **D**) Voltage-clamp traces of neurons from VTA slice preparations in response to repeated 200-ms NIR stimulation. NIR light triggered photocurrents only in HUP-treated neurons. a, b, and c show the voltage-clamp traces of three independent neurons. (**E**) Current-clamp traces of an HUP-treated VTA neuron in response to trains of NIR pulses at 10-ms (left) and 40-ms (right) pulse durations at 2 Hz. (**F**) Left, current-clamp traces of an HUP-treated MS neuron in response to trains of 15-ms NIR pulses at 2 Hz. Right, voltage-clamp traces of neuron from MS slice preparations in response to 15-ms NIR stimulation at 2 Hz. NIR light triggered photocurrents in HUP-treated MS neuron. (**G**) Current-clamp traces of an HUP-treated mPFC neuron in response to trains of 10-ms NIR pulses at 2 Hz. (**H**) Current-clamp traces of an HUP-treated ACC neuron in response to trains of 15-ms NIR pulses at 2 Hz. Brief red lines indicate NIR pulses.

validate the efficacy of HUP, we extended our investigation to the medial prefrontal cortex (mPFC) and anterior cingulate cortex (ACC) regions. The results demonstrated that neurons in the mPFC and ACC were excited by NIR light in conjunction with HUP (Fig. 3, G and H, and fig. S10). These findings strongly support our hypothesis that HUP can activate neurons without genetic modification.

We note that the spike probability could exceed 100% (fig. S11), suggesting that our HUP method intensifies neural excitation beyond traditional optogenetics (*57*–*59*), where the probability typically does not exceed one spike per pulse. This difference arises from distinct excitation mechanisms: Whereas optogenetics relies on light-sensitive proteins with limited quantum yield, HUP generates an electric field driving ion flux in the extracellular space. To investigate this effect with single pulses, we conducted additional experiments revealing that, among 18 trials across three neurons previously showing >100% spike probability with periodic stimulation at 2 Hz, 14 trials (78%) yielded multiple spikes (mean: 2.8 ± 0.5, range 1 to 10) (fig. S12). This phenomenon arises from the photocurrent's delayed decay (Fig. 2G), likely due to charge detrapping in $WO_{3-x}$ defect states (*60*) and capacitive discharge at the electrode-electrolyte interface (*61*, *62*), thus enabling multiple action potentials per pulse. The resulting sustained inward currents (Fig. 3, C and D) further suggest a

slower restoration of ionic equilibrium near the neuronal membrane, prolonging the effective stimulus.

### In vivo validation of HUP neuromodulation in MS area

To demonstrate the effectiveness of optoelectronic stimulation via our HUP system in vivo, we first selected the MS as a representative deep brain region, which is integral to regulating neural activity within the hippocampus (*63*). We conducted in vivo electrophysiological recordings using a chemically induced epilepsy model to evaluate the efficacy of HUP in inhibiting neural activity. We administered HUP into the MS region and implanted electrodes arrays within the hippocampus (Fig. 4A). From the electron microscopy image, the close spatial arrangement of spherical UCNPs with $WO_{3-x}$ nanorods ensured efficient blue light absorption (Fig. 4B). Seven days postinjection, awake mice were administered kainic acid (KA) to induce seizures, with strong oscillations evident in the recorded local field potential (LFP) from the hippocampus (Fig. 4C, bottom left, and fig. S13).

Transcranial pulsed NIR irradiation (15-ms pulses at 8 Hz, 60 s, 1.2-W peak power, and 15.7 W/cm$^2$) reduced seizure activity immediately following stimulation, demonstrating the silencing of hippocampal neurons by HUP (Fig. 4C, top left). In contrast, no clear differences were observed in the spectra of the control group mice injected only with UCNPs or $WO_{3-x}$ before and after the light stimulation (Fig. 4C, right). Similar seizure suppression was also observed

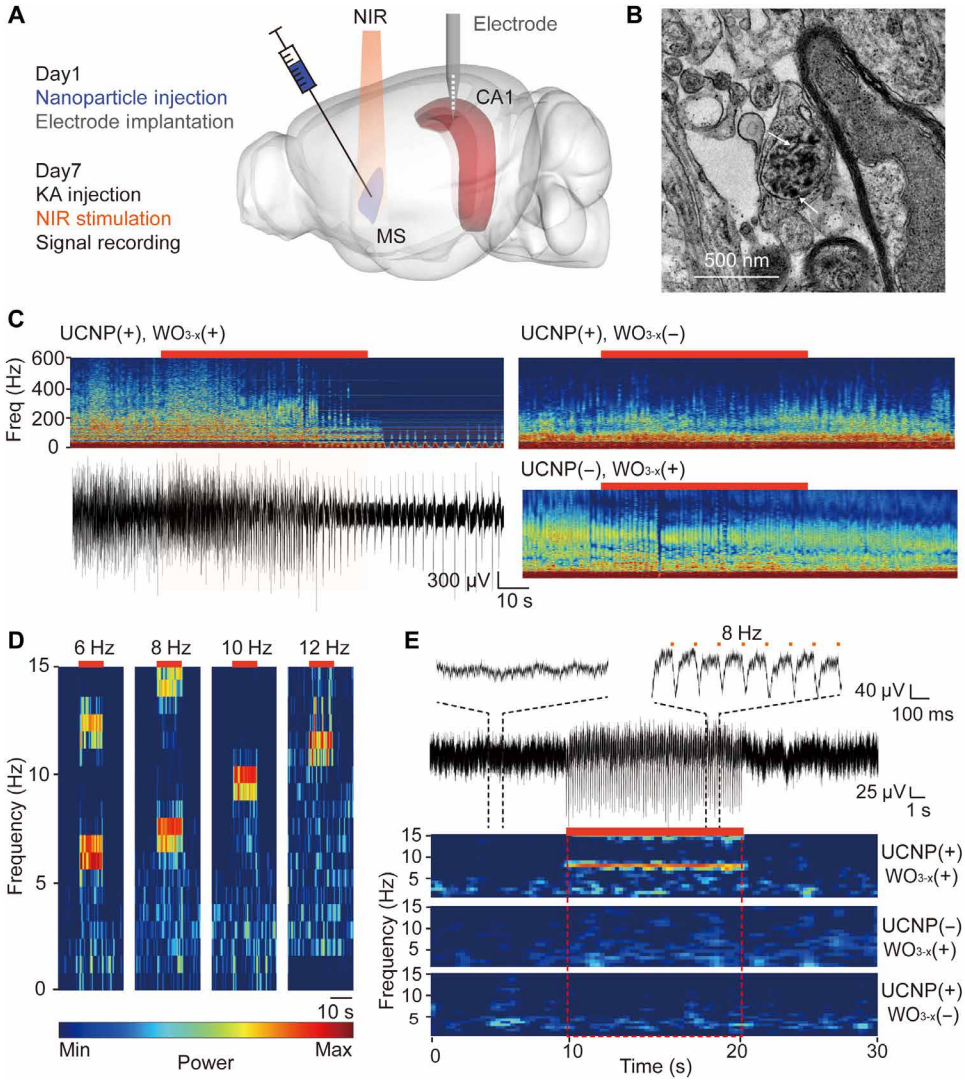


**Fig. 4. NIR excitation of MS region in vivo.** (**A**) Experimental scheme for NIR excitation of the MS. On day 1, 3.75 μl of nanoparticles (200 mg/ml) were injected into the MS, and electronic neural probes were implanted targeting the hippocampus area. On day 7, for the seizure suppression experiment, KA (15 mg/kg) was administered to induce seizures; for the neural synchronization experiment, KA was not used. (**B**) TEM image of HUP within MS tissue. White arrows indicate clusters of HUP. (**C**) Hippocampal LFP response to transcranial NIR stimulation (15-ms pulses at 8 Hz, 60 s, 1.2-W peak power, 15.7 W/cm$^2$, and 144-mW average power) in mice with different nanoparticle injections. Left: LFP from mice with HUP injection showing weakened oscillations post-excitation. Power spectrum analysis indicates a decrease in high-frequency components, suggesting seizure suppression. Right: Power spectra from mice injected only with UCNPs or $WO_{3-x}$ show no clear change in the LFP spectra before and after NIR irradiation. Brief red lines indicate NIR irradiation. (**D**) Synchronization of hippocampal LFP in a frequency-dependent manner, with excitation pulses at 6, 8, 10, and 12 Hz. (**E**) Hippocampal LFP response to 8-Hz NIR stimulation (15-ms pulses, 10 s, 1.2-W peak power, 15.7 W/cm$^2$, and 144-mW average power) under different conditions. Top: raw LFP trace from a mouse with HUP injection. Bottom: power in the theta range averaged across 30-s trials for HUP, UCNPs, and $WO_{3-x}$ conditions.

in another four independent mice. The electrophysiological plots from these animals are presented in fig. S14.

Furthermore, we explored the potential of HUP for noninvasive synchronization of neural activity. Directed NIR stimulation toward neurons in the MS revealed that pulsed NIR at theta frequencies (6 to 12 Hz) effectively synchronized hippocampal theta oscillations dependent on the frequency of optical stimulation (Fig. 4D). For instance, 80Hz stimulation showed clear modulation in the LFP recordings and spectral power distribution, as depicted in Fig. 4E. Control animals receiving only UCNPs or $WO_{3-x}$ injections displayed no such synchronization under NIR irradiation, highlighting HUP's unique capability to noninvasively modulate neural circuitry. Similar synchronization was observed in three additional independent mice, as shown in fig. S15. These results confirm that the observed synchronized theta oscillations are induced by HUP-mediated NIR stimulation as these narrow oscillations at specific frequencies are unnatural for mice.

We note that although the effects of HUP injection may occur immediately as demonstrated in the in vitro experiment, the 1-week interval was chosen to allow for recovery following the implantation of the rigid 32-channel probe before recording. In addition, we confirmed the rapid response of HUP-based neuromodulation by applying it to the motor cortex, where turning behaviors were observed in mice with HUP injection upon NIR irradiation, in contrast to no response in the control group (fig. S16).

This 1-week waiting period is also consistent with our findings that HUP remains confined near the injection site without extensive diffusion within 3 weeks postinjection, with a typical distribution radius of approximately 50 to 100 μm (fig. S17). Notably, this confinement was consistent across injection volumes ranging from 0.5 to 3 μl (fig. S18), suggesting that the nanoparticles tend to deposit immediately after exiting the needle at the slow injection speed used. Furthermore, electron microscopy images revealed that the HUP components primarily remained on the neuronal surface (Fig. 4B and fig. S19). The confined HUP localization also enhances the spatial precision of this stimulation approach. Using a COMSOL-based numerical simulation (*64*), we modeled the current density distribution around a single nanoparticle (~100 nm), finding that the photocurrent drops by five orders of magnitude within 20 μm (fig. S20). This steep decline ensures high spatial resolution, restricting the electrical stimulus to the nanoparticle region even under a broader 0.9-mm full width at half maximum (*FWHM*) illumination (fig. S21). Together, the confined HUP localization and rapid photocurrent decay contribute to the precision of this approach.

We also used immunofluorescence histology to quantify the effectiveness of NIR stimulation at the sites injected with HUP. Neuronal activation was determined by imaging the expression of c-Fos, a well-established biomarker for neuronal activity that peaks approximately 1 to 2 hours poststimulation, alongside 4′,6-diamidino-2-phenylindole (DAPI) staining. As depicted in Fig. 5 (A and B), neuronal excitation in the MS region was effectively triggered by NIR irradiation only in the presence of HUP, as evidenced by a substantially elevated proportion of c-Fos–positive cells, up to 20% of DAPI-stained cells. In contrast, negligible c-Fos expression was observed in any of the control groups lacking either NIR irradiation, UCNPs, or $WO_{3-x}$ (Fig. 5, A and C).

### In vivo validation of HUP neuromodulation in VTA

After examining the MS region, we turned our attention to the VTA area, which is crucial for dopamine release and directly linked to behaviors associated with preference choice and major depression (*65*–*69*). Current stimulation methods, such as optogenetics, electrical, and thermal stimulation, can activate this region (*10*, *18*, *70*). However, precise, noninvasive optical stimulation of the VTA in wild-type mice has not yet been explored (Fig. 6A). To demonstrate the effectiveness of our HUP system for optoelectronic stimulation in the VTA, we used a combination of chronic behavioral tests and acute electrochemical assays.

Initially, we assessed the effectiveness of VTA activation using a behavioral experiment. To minimize the impact of injection on the mice's behavior, behavioral tests were conducted 7 days postinjection. After contextual training with NIR neuromodulation [1.2 W peak power, 15-ms pulse duration at 20 Hz and 39.2 W/cm$^2$, 1 s on every 10 s the mice spent in the region of interest (ROI)] for three consecutive days, mice with HUP injection in the VTA exhibited a strong preference for the NIR-illuminated arm terminal, spending up to 78% of the time there on average in the posttest as shown in Fig. 6 (B and C). This result demonstrates the capability of deep-brain optical neuromodulation without the use of any optogenetics or implanted electronics in freely behaving animals. Moreover, the specificity of in vivo NIR neuromodulation of VTA neurons was validated by comparing it to nonirradiated, UCNPs, and $WO_{3-x}$ control groups, where the mice spent about 30% of the time in any of the three arms with less preference (Fig. 6C).

We further conducted quantitative, real-time electrochemical detection of dopamine release, a key marker of VTA activation, as illustrated in Fig. 6D. Our setup enabled the real-time measurement of dopamine. Striatal dopamine transients reflect the activity of VTA dopamine neurons, which is relevant for developing therapeutic strategies against major depression. Dopamine concentration was quantified by the current amplitude at the characterized oxidation peak (fig. S22) in the current-time scan curve from the electrochemical workstation via optical stimulation. The relative increase in current amplitude upon NIR irradiation was used to quantify the relative amount of dopamine (see the Supplementary Materials for details). In mice with HUP injection in the VTA, dopamine release was immediately detected following NIR optical stimulation (15-ms pulses at 20 Hz, 1.2-W peak power, 39.2 W/cm$^2$, and lasts 10 s). After 10 s of NIR stimulation, striatal dopamine release comes to decrease (Fig. 6E). In contrast, no notable dopamine release was detected in control mice lacking NIR stimulation or those with only UCNPs or $WO_{3-x}$ injections. The cumulative dopamine release in the HUP-treated mice enhanced significantly compared with control mice with omission of NIR stimulation, UCNPs injection, or $WO_{3-x}$ injection, demonstrating the effectiveness of our optoelectronic neural stimulation (Fig. 6F).

Similar neuronal patterns of activation were observed in the immunofluorescence histology of VTA region (Fig. 7A). Mice with HUP injection and subjected to NIR irradiation displayed a marked increase in c-Fos expression (Fig. 7B). Conversely, control mice lacking one of the essential components–UCNPs, $WO_{3-x}$, or NIR stimulation–showed no significant c-Fos expression in the VTA (Fig. 7C).

We note that the control experimental results under conditions with NIR irradiation but lacking either UCNP or $WO_{3-x}$ also confirm that the observed neuromodulation arises from the photovoltaic effect rather than potential thermal effects of NIR irradiation. To further rule out thermal effects, we performed in vivo temperature measurements in the MS target brain region. Our measurements showed only mild temperature increases of less than 1°C

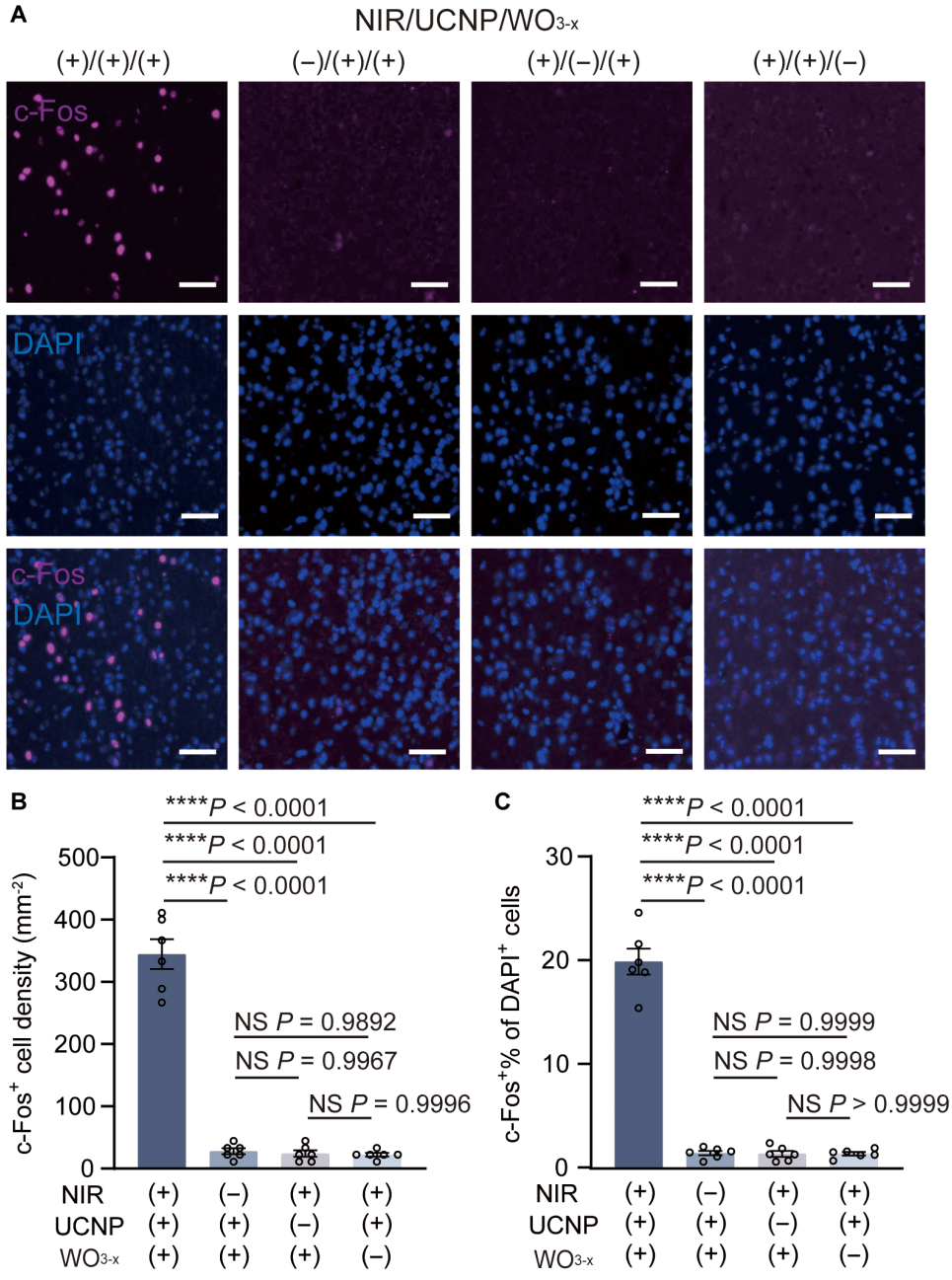


**Fig. 5. Immunohistology of the MS region after NIR illumination.** (**A**) Representative images showing the MS region under different experimental conditions. A notable increase in c-Fos expression driven by NIR stimulation was observed only in the presence of HUP. Scale bars, 50 μm. (**B**) Statistical analysis of the density of c-Fos$^+$ cells in the MS regions for the four conditions. (**C**) Statistical analysis of the percentage of c-Fos$^+$ cells within the DAPI population in the MS regions for the four conditions. All data are presented as means ± SEM. $n = 6$ mice per group. All data passed the Shapiro-Wilk normality test. One-way analysis of variance (ANOVA) with Tukey's multiple comparisons test was applied for statistical analysis. $P$ values are labeled in the figure. Significant differences ($P < 0.05$) appear only when comparing the complete HUP + NIR group to any of the control groups. No significant differences were observed among the control groups. ****$P < 0.0001$; NS, not significant.

under the experimental conditions used in this study (Supplementary Materials, fig. S23, and table S1). Such temperature changes are insufficient to activate wild-type neurons (*18*, *71*). However, at higher laser powers, careful optimization of NIR parameters–including power, pulse duration, frequency, and exposure period–is essential to ensure effective stimulation while minimizing the risk of thermal damage to tissues.

## DISCUSSION

As a proof of concept, our study demonstrates that by integrating upconversion with photovoltaic effects in a single system, HUP not only eliminates the need for optogenetics, commonly required in UCNP-based neuromodulation, but also extends the spectral range of photovoltaic-based neuromodulation into the NIR region, allowing for noninvasive deep brain stimulation. Such capabilities mark a

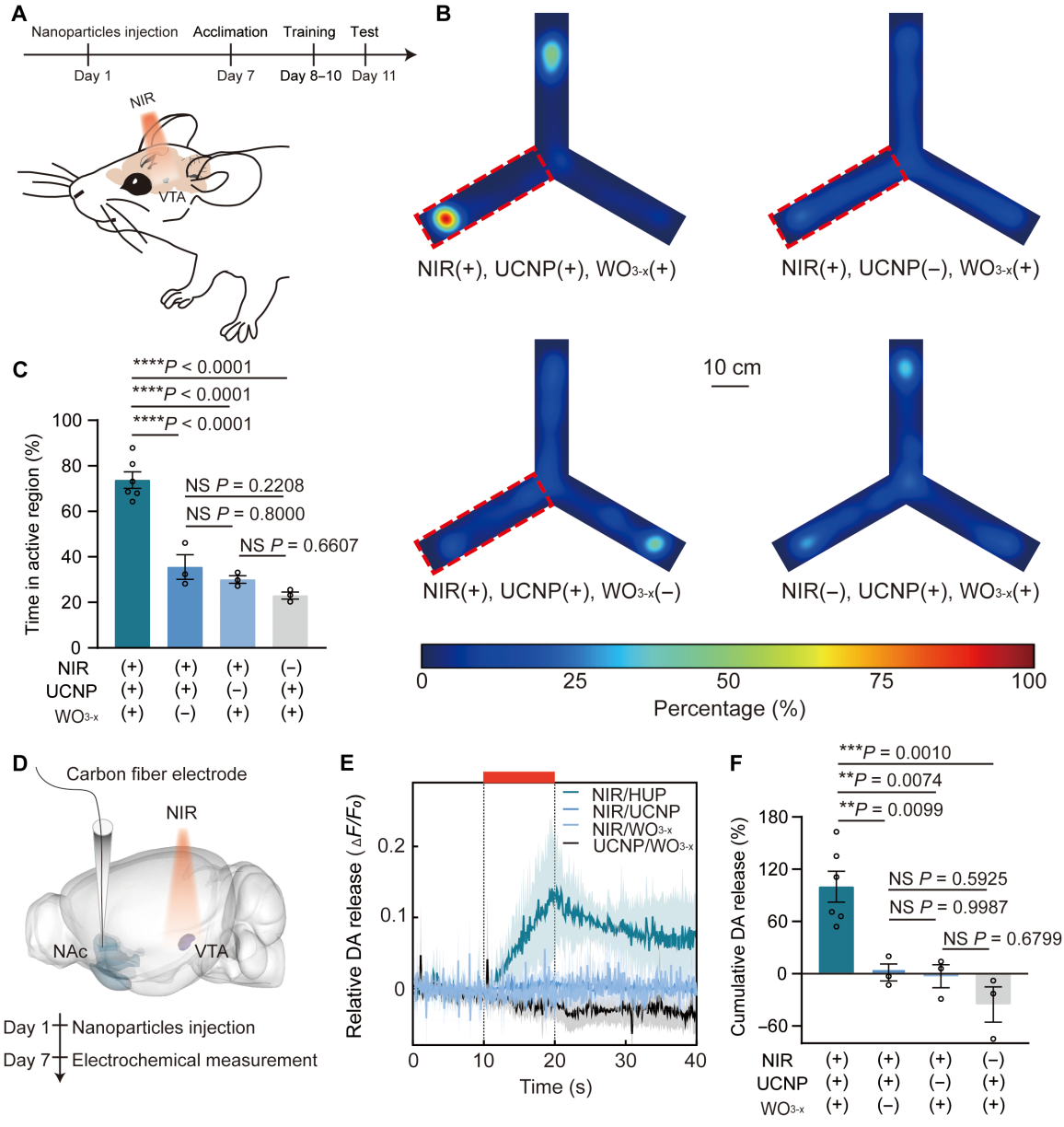


**Fig. 6. NIR excitation of VTA region in vivo.** (**A**) Experimental setup for transcranial NIR stimulation of the VTA in mice. The schematic illustrates the HUP injected mouse stimulated by NIR irradiation. (**B**) Heatmaps depicting the movement patterns of mice under various conditions for NIR(+)/UCNP(+)/$WO_{3-x}$(+), NIR(+)/UCNP(+)/$WO_{3-x}$(−), NIR(+)/UCNP(−)/$WO_{3-x}$(+), and NIR(−)/UCNP(+)/$WO_{3-x}$(+), respectively. The red dashed boxes indicate areas where entering triggers NIR irradiation. (**C**) Statistical analysis of the duration mice spent in NIR-illuminated areas, comparing different combinations of NIR, UCNPs, and $WO_{3-x}$ in the VTA. (**D**) Schematic of the experimental approach for in vivo electrochemical measurement of dopamine (DA) transients in the ventral striatum during NIR stimulation of the VTA. (**E**) Graph showing relative changes in DA concentration in the ventral striatum in response to transcranial VTA stimulation under different experimental conditions. (**F**) Statistical analysis of cumulative DA release within 30 s after initiating transcranial stimulation under the four conditions illustrated in (E), highlighting significant DA release only in the presence of HUP and transcranial NIR irradiation. All data in (C), (E), and (F) are presented as means ± SEM, with $n = 6$ mice for NIR(+)/UCNP(+)/$WO_{3-x}$(+) and $n = 3$ mice for all other groups. For statistical analysis in (C) and (F), all data passed the Shapiro-Wilk normality test. One-way ANOVA with Tukey's multiple comparison test was applied for statistical analysis. *P* values are labeled in the figure. Significant differences ($P < 0.05$) appear only when comparing the complete HUP + NIR group to any of the control groups. No significant differences were observed among the control groups.

substantial advancement over traditional methods like optogenetics and electrical implants, which are restricted by their need for light-activated proteins and inherent invasiveness. HUP excels in modulating neural activity within deep brain regions such as MS and VTA, which are essential for cognitive and emotional processing. Furthermore, the versatility of the HUP method suggests promising applications beyond these areas, potentially extending its transformative approach to broader neural networks including the cortex and peripheral nerves, paving the way for its adoption in a wide range of neurological therapeutic strategies.

Noticeably, to excite a specific brain region, traditional optogenetic approaches require the injection of a virus into the desired area

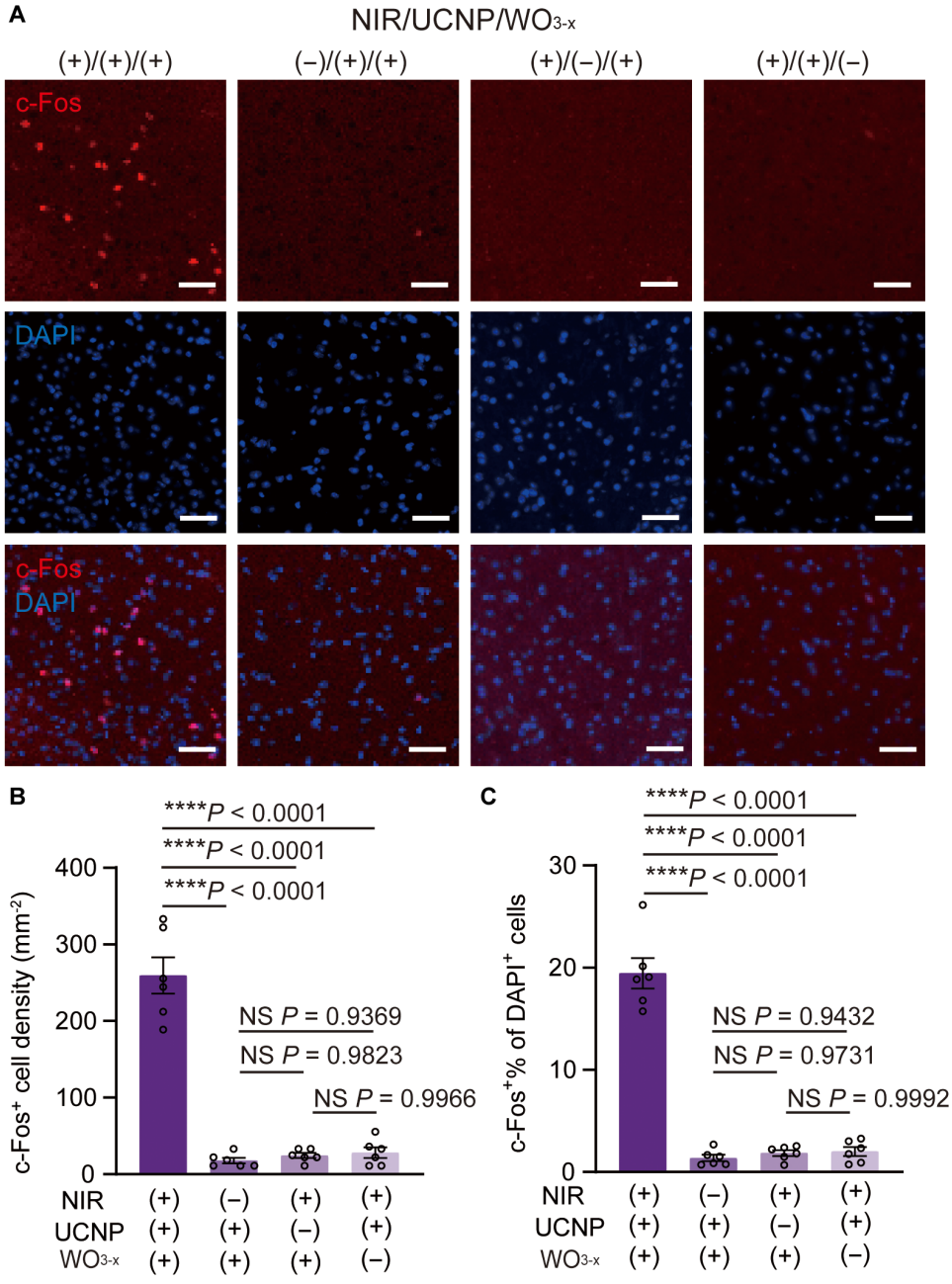


**Fig. 7. Immunohistology of the VTA region after NIR illumination.** (**A**) Representative images showing the VTA region under different experimental conditions. A notable increase in c-Fos expression driven by NIR stimulation was observed only in the presence of HUP. Scale bars, 50 μm. (**B**) Statistical analysis of the density of c-Fos$^+$ cells in the VTA regions for the four conditions. (**C**) Statistical analysis of the percentage of c-Fos$^+$ cells within the DAPI population in the VTA regions for the four conditions. All data are presented as means ± SEM. $n = 6$ mice per group. All data passed the Shapiro-Wilk normality test. One-way ANOVA with Tukey's multiple comparisons test was applied for statistical analysis. *P* values are labeled in the figure. Significant differences ($P < 0.05$) appear only when comparing the complete HUP + NIR group to any of the control groups. No significant differences were observed among the control groups. ****$P < 0.0001$; NS, not significant.

and a subsequent transfection and recovery period of at least 3 weeks before experiments can commence. In contrast, our HUP method allows for an immediate response upon optical excitation, substantially simplifying and accelerating the experimental procedures required for fundamental neuroscience research. This capability not only saves valuable time but also reduces the complexity of the experiments, making it a highly efficient alternative.

We also note that UCNPs have previously been used for deep brain stimulation. However, unlike traditional UCNP-based neuromodulation methods that primarily rely on optogenetics or UV-sensitive agonists such as transient receptor potential ankyrin-repeat 1 (TRPA1) channels, our approach does not depend on genetic modification or receptor-specific limitations. For example, TRPA1 activation is largely restricted to nociceptive neurons (*72*), which narrow its

applicability to other neuronal types and networks. By contrast, our HUP system uniquely combines UCNPs and photovoltaic materials to convert NIR light directly into electric stimuli, enabling precise and targeted stimulation in deep-brain regions. This innovation greatly expands the range of neural populations and species that can be studied or treated, offering broader applications compared to earlier methods.

There are several areas where HUP technology could be further improved. First, systematic optimization of both the HUP injection dose and the NIR stimulation parameters is crucial for enhancing accuracy and safety. For example, adopting a focused light spot could further improve spatial stimulation precision and reduce the required laser power. Second, developing more efficient upconversion and photovoltaic materials is critical. For instance, better aligning the UCNP emission band with the photovoltaic interband transition could substantially improve NIR neuromodulation efficacy. Future advancements might involve integrating the heterogeneous materials into a single entity rather than the current approach of mixing, potentially offering more stable and efficient photovoltaic conversion and stimulation. Lastly, the development of targeted nanoparticle delivery methods to specific cells or brain regions would be revolutionary. This could include surface modifications of the materials (*73*, *74*) or the use of external fields (*75*, *76*), such as ultrasound and magnetic field, to drive nanoparticles across the blood-brain barrier (*77*), enhancing the specificity and effectiveness of the stimulation. With these methods, the HUP technology may extend beyond basic neuroscience research to potentially revolutionize treatments for neurological disorders such as epilepsy, depression, and Parkinson's disease. Its noninvasive nature and precision hold promises for patient-friendly therapies that minimize neurosurgical risks and improve recovery times.

## MATERIALS AND METHODS

### Synthetic reagents

$WCl_6$ (99.9%), $YCl_3{\cdot}6H_2O$ (99.9%), $YbCl_3{\cdot}6H_2O$ (99.9%), $TmCl_3{\cdot}6H_2O$ (99.9%), $NH_4F$ (98%), NaOH (97%), polyvinylpyrrolidone (PVP, ribonuclease-free PVP K30 solution, 30%), TEOS (98%), ammonia aqueous (25 to 28%), oleic acid (OA, 90%), 1-octadecene (ODE, 99%) cyclohexane (99.5%), methanol (99.5%), and ethanol (99.8%) were purchased from Aladdin and without further purification.

### Synthesis of $NaYF_4$:30%Yb/0.05%Tm UCNPs

The uniform nanoparticles $NaYF_4$:30%Yb/0.05%Tm were synthesized by the coprecipitation method. A typical procedure is as follows: $YCl_3{\cdot}6H_2O$ (0.695 mmol), $YbCl_3{\cdot}6H_2O$ (0.3 mmol), and $TmCl_3{\cdot}6H_2O$ (0.005 mmol) were added into a 100-ml three-necked flask containing 6 ml of OA and 15 ml of ODE. The mixture was first heated to 150°C under argon for 30 min to form a transparent solution. The solution was cooled down to room temperature, and 8 ml of a methanol solution containing NaOH (2.5 mmol) and $NH_4F$ (4 mmol) was slowly dropped into the flask and stirred for 30 min. Then, the solution was heated to 80°C and maintained for 20 min to evaporate methanol. The solution was heated to 150°C to evaporate water. Subsequently, the solution was heated to 300°C and maintained for 1.5 hours under argon atmosphere. After cooling down to room temperature, the resulting products were precipitated by ethanol and collected by centrifugation at 7000 rpm for 3 min. The precipitate was then purified with methanol and ethanol three times and finally dispersed in cyclohexane for further use.

### $NaYF_4$ shell precursors

Firstly, 1 mmol $YCl_3{\cdot}6H_2O$ were added to a 100-ml flask containing 6 ml of OA and 15 ml of ODE. The mixture was heated to 150°C under argon for 30 min to form a transparent solution and then cooled down to room temperature, and 8 ml of a methanol solution containing NaOH (2.5 mmol) and $NH_4F$ (4 mmol) was slowly dropped into the flask and stirred for 20 min. Then, the solution was heated to 80°C to evaporate methanol. The solution was heated to 150°C for 10 min. Last, the reaction solution was cooled down to room temperature as $NaYF_4$ shell precursors.

### Synthesis of $NaYF_4$:Yb/tm@$NaYF_4$

The epitaxial growth of $NaYF_4$:Yb/Tm@$NaYF_4$ to form a core-shell structure was realized by a hot-injection method. The nanoparticles $NaYF_4$:Yb/Tm (0.4 mmol) core samples were added to a 100-ml flask containing 3 ml of OA and 8 ml of ODE. The mixture was heated to 300°C. After that, 2 ml of $NaYF_4$ shell precursors were injected into the reaction mixture step by step with an injection rate of 0.2 ml every 3 min. After the injection of 2 ml of $NaYF_4$ shell precursors, the reaction solution was cooled down to room temperature, and $NaYF_4$:Yb/Tm@$NaYF_4$ nanocrystals were washed with cyclohexane, ethanol, and methanol.

### Synthesis of $NaYF_4$:Yb/tm@$NaYF_4$@$SiO_2$ nanoparticles

Two milliliter of PVP, 0.1 mmol of $NaYF_4$:Yb/Tm@$NaYF_4$ nanoparticles, and 30 ml of cyclohexane were added in a flask and stirred for 10 min. Then, 0.2 ml of ammonia aqueous was added and sonicated for 10 min. TEOS (0.03 ml) was added into the solution, and the reaction process was completed by stirring the solution at 500 rpm for 12 hours. The obtained $NaYF_4$:Yb/Tm@$NaYF_4$@$SiO_2$ nanoparticles were washed with ethanol and finally dispersed in ethanol for future use.

### Synthesis of $WO_{3-x}$

$WO_{3-x}$ nanowire was synthesized according to a solvothermal method by using absolute ethanol as the solvent. Typically, 0.5 g of $WCl_6$ was dissolved in 100 ml of absolute ethanol to form a transparent yellow solution. Then, the above solution was equivalently transferred into two 100-m Teflon-lined stainless-steel autoclaves and heated at 180°C for 24 hours. Last, the $WO_{3-x}$ precipitate was obtained by purifying with DI water and absolute ethanol three times and dried in oven overnight.

### Preparation of HUP

HUP was prepared by mechanistically grinding UCNPs and $WO_{3-x}$ with a mass ratio of 1:1.

### TEM imaging of UCNPs, $WO_{3-x}$, and HUP

The TEM images were all collected on TALOS F200X with an accelerating voltage of 200 kV.

### Dynamic light scattering of UCNPs

The hydrodynamic sizes of UCNPs were tested by using dynamic light scattering on Malvern Nano-ZS Particle Sizer.

### UV-vis-NIR absorption spectroscopy of $WO_{3-x}$

The UV-vis diffuse reflectance spectra were recorded on a Lambda 750 UV/vis spectrometer.

### Photocurrent measurement

The photocurrent measurements were performed with a three-electrode system in PBS (pH 7.2) under the irradiation of 980-nm laser of 26 W/cm$^2$. The working electrodes were prepared by uniformly drop-casting the slurry of $WO_{3-x}$ or HUP onto the fluorine-doped tin-oxide (FTO) glass (1 cm by 1 cm) and calcined in air at 200°C for 2 hours. The counter electrode and reference electrode were Pt wire and Ag/AgCl, respectively.

### Photoluminescence measurement

The UCNP stock solution was prepared. Firstly, 5 mg of UCNPs were taken into a 500-μl centrifuge tube. Subsequently, 25-μl of PBS was added in the 500-μl centrifuge tube. Next, the mixed solution was sonicated for 5 min and prepared for the next step: preparation of the $WO_{3-x}$ stock solution. Five milligram of $WO_{3-x}$ was taken into a 500-μl centrifuge tube. Then, 25 μl of PBS was added in the 500-μl centrifuge tube. Subsequently, the mixed solution was sonicated for 5 min.

Mixed solutions of UCNP and $WO_{3-x}$ were prepared using their respective stock solutions. UCNP and $WO_{3-x}$ were mixed in the following ratios: 1:9, 3:7, 5:5, 7:3, and 9:1. First, 5 μl of UCNP stock solution was taken into a 200-μl centrifuge tube by using a pipettor. Subsequently, 45 μl of $WO_{3-x}$ stock solution was added in the 200-μl centrifuge tube. Next, the mixed solution was sonicated for 5 min. Following this, the mixed solution was taken from the 200-μl centrifuge tube into a "well" of the 96-well culture plate and was sealed by using a quartz coverslip. The preparation steps for mixed solutions of UCNP and $WO_{3-x}$ in other ratios were consistent with those described above.

The mixed solution in the well of the 96-well culture plate was placed on the stage of the micro-Raman spectrometer (LabRAM HR Evolution, ideaoptics). The excitation wavelength and the power of the laser were 980 nm and 1 mW, respectively. The imaging magnification of the objective lens used to acquire the upconversion luminescence spectra is 10×.

### Animal subjects

All mice were aged between 8 and 10 weeks before commencement of experiments and were maintained on a 12-hour light-dark cycle with ad libitum access to food and water. Neonatal rats were used for primary cell culture. We used wild-type C57BL/6J mice and Sprague-Dawley obtained from Phenotek Biotechnology Co. Ltd. All our animal experiments obtained ethical approval from the Ethics Committee for Animal Management at the Phenotek Biotechnology (approval numbers 20240708-01 and AUP-20250123-01). Our experimental conditions and handling procedures for mice complied with the ethical requirements for experimental animals. Mice were randomly assigned to each experimental group before treatment. For behavioral experiments, each experiment was successfully repeated at least two times.

### Injection of nanoparticles

In vivo nanoparticles were performed using the brain stereoscope to locate the MS region [anteroposterior (AP): +0.9 mm, mediolateral (ML): +0.1 mm, and dorsoventral (DV): −4.1 mm] or VTA region (AP: −3.1 mm, ML: +0.4 mm, and DV: −4.2 mm). First, all the surgical subjects were sterilized with 70% ethanol and rinsed with sterile DI water and sterile 1× PBS before use. UCNPs or $WO_{3-x}$ were dispersed in sterile 1× PBS before injection. Then, the mice were anesthetized by isoflurane and the head hair of the mouse was removed by the blade and iodophor was applied to sterilize the exposed scalp skin. Erythromycin ointment was applied on both eyes of the mouse to moisturize the eye surface and prevent the eyes from light exposure throughout the surgery. The mice were placed in the stereotaxic frame (RWD) equipped with two ear bars and one nose clamp that fix the mouse head in position. The mouse skull was fully exposed by surgical scissors without any skin removal. Three % hydrogen peroxide was used to remove the mucosa under the scalp skin. For each animal, depending on the targeted brain region, a 0.5-mm-diameter burr hole was drilled using a dental drill according to the AP and ML coordinates described above. UCNP (3.75 μl) (5 mg of UCNPs dispersed in 50 μl of PBS), $WO_{3-x}$ (5 mg $WO_{3-x}$ dispersed in 50 μl of PBS), or HUP (5 mg UCNPs and 5 mg $WO_{3-x}$ dispersed in 50 μl of PBS) solution was injected at 0.375 μl/min into MS or VTA region of the brain using a microsyringe pump (Pump 11 Elite, Harvard Apparatus) with a 33-gauge needle. The injection syringe should stay in the located brain tissue for 10 min to insure the full diffusion of the nanoparticles before withdrawal.

### In vitro whole-cell patch-clamp recording under NIR stimulation

Trace amount of HUP, UCNPs, or $WO_{3-x}$ solution were injected on the brain slice prepared using a vibratome (Leica). Slices were incubated at 32°C in oxygenated artificial cerebrospinal fluid (ACSF) with the following composition: 125 mM NaCl, 2 mM KCl, 2 mM $CaCl_2$, 1.3 mM $MgSO_4$, 1.3 mM $NaH_2PO_4$, 12 mM glucose, and 26 mM $NaHCO_3$. The incubation lasted for at least 1 hour before recordings. Slices were transferred to a recording chamber and superfused with ACSF at a flow rate of 2 ml/min. Whole-cell current- and voltage-clamp recordings were conducted using an EPC10 amplifier and PatchMaster 2.54 software (HEKA, Lambrecht, Germany). Patch pipettes with a resistance of 3 to 4 megohm were filled with an internal solution containing 140 mM K-Gluconate, 0.1 mM $CaCl_2$, 2 mM $MgCl_2$, 1 mM EGTA, 2 mM K2–adenosine 5′-triphosphate (ATP), 0.1 mM Na3-ATP, and 10 mM Hepes (pH adjusted to 7.3 with KOH, 290 mOsm kg$^{-1}$). Neurons were held at −50 ~ −70 mV in voltage-clamp mode to record evoked action potentials. Cells were randomized into different experimental groups.

### In vitro TEM of nanoparticles in brain

HUP (3.75 μl of 200 mg/ml) was injected bilaterally into mouse MS. Three days after UCNP injection, the mice were transcardially perfused with 4% paraformaldehyde (PFA)/1% glutaraldehyde in 0.1 M PBS at 10 ml/min. The brains were postfixed in 2.5% glutaraldehyde in 0.1 M PBS overnight at 4°C, and 100 μm-thick vibratome sections were prepared on a vibratome (VT1000S, Leica). After washing three times with 0.1 M PBS, the sections were postfixed with 100 μl of 1% osmic acid for 1.5 hours and washed three times with double distilled water for 10 min each. Thereafter, the sections were dyed with 100 μl of 2% uranium acetate for 30 min and dehydrated through graded ethanol series of 50, 70, and 90% for 15 min each and 100% for 20 min twice. The sections were treated with 100% acetone for 20 min and then immersed in freshly prepared Durcupan resin overnight. After embedding and resin curing, the MS region was excised out from the embedded sections and glued onto resin block for ultrathin sectioning. Seventy-nanometer ultrathin sections were cut with a diamond knife (Diatome) using a Reichert-Jung ultracut E ultramicrotome, collected in formvar-coated single-slot copper grid, and briefly counterstained with 2% uranyl acetate in 50% ethanol and 0.4% lead citrate. The sections were observed under electron microscope (Tecnai G2 spirit 120 kV), and images were captured using a CCD camera (Gatan 832).

### In vitro two-photon photoluminescence imaging of HUP distribution

To assess the distribution of HUP over time, we injected HUP (mass ratio of UCNP:$WO_{3-x}$ = 2:1 for better fluorescence brightness) into the MS region of the mice. Brain dissections were performed at 7, 14, and 21 days postinjection. Slices of 1-mm thickness were analyzed using a two-photon imaging microscope (Bruker) with an excitation wavelength of 980 nm and a blue-channel band-pass filter corresponding to the emission peak of UCNPs at 450 nm.

### Scanning electron microscopy imaging of in vitro primary cell

Wild-type Sprague-Dawley rats were used for primary cultures. Primary cortical neurons isolated and prepared from neonatal rat brain tissue, seeded onto glass coverslips in a 24-well plate, and cultured at 37°C in a 5% $CO_2$ incubator for 6 days. Subsequently, 10 μl of HUP nanoparticles solution at a concentration of 2 mg/ml was carefully applied to four edges and the central region of each coverslip (total 50 μl). The cultures were then incubated under the same conditions for an additional 2 hours. Following incubation, the cells were fixed with 2.5% glutaraldehyde for 1 hour. After fixation, a graded ethanol dehydration series (30, 50, 70, 80, 90, and 95%) was performed, with each step lasting 15 in. The samples were further dehydrated in 100% anhydrous ethanol for 20 min and then immersed in acetone for another 20 min to ensure complete dehydration and removal of residual substances. The samples were subsequently air-dried naturally. To enhance electrical conductivity, a platinum (Pt) layer with a thickness of 2 nm was sputtered onto the sample surfaces. Last, the surface morphology of the samples was characterized using a S4800 field emission scanning electron microscopy (Hitachi, Japan).

### Numerical simulation of the current density distribution

A three-dimensional (3D) finite element model was developed using COMSOL Multiphysics to evaluate the high spatial resolution of neural stimulation in the HUP system. The simulation analyzed the current density distribution in brain tissue when an HUP delivered electrical stimulation. Brain tissue was modeled as a sphere with a diameter of 100 μm, while the HUP was represented as a sphere with a diameter of 100 nm. The surface of the HUP was assigned a constant current source boundary condition, whereas the surface of the brain tissue was set as ground. The brain tissue's electrical conductivity was set to 0.2 S/m, and the relative permittivity was set to 88.9.

### Laser beam spot size measurement by knife-edge method and average power density calculation

The laser beam spot size was determined using the knife-edge method. A knife edge, positioned 6 mm from the fiber output and perpendicular to the beam, was moved along the transverse direction ($x$ axis) using a high-precision translation stage (10-μm accuracy). A large-area photodetector measured the transmitted optical power as a function of knife-edge position, producing an S-shaped curve of power versus position. The data were fitted with an error function to derive the *FWHM*. For a pulsed laser, the average power density was calculated as

$$Average\ power\ density = \frac{2 \times Power \times Pulse\ duration \times Repetition\ rate}{\pi w^2} \quad (1)$$

with

$$w = FWHM/1.177 \quad (2)$$

### Surgery of creating cranial window

All surgeries were performed using a stereotaxic frame from RWD Life Science Co., Ltd. (RWD). Mice were anesthetized with isoflurane gas, administered via a desktop animal anesthesia machine from RWD. Scalp incision and craniotomy were performed at the designated coordinates for MS or VTA brain regions. A circular hole, approximately 5 mm in diameter, was drilled in the skull over the target brain region. A circular glass coverslip of the same diameter (5 mm) was placed over the hole, with the edges sealed to the skull using either 3M VetBond tissue adhesive or Kwik-Cast silicone sealant. METABOND dental cement (Parkell) was applied to secure the glass coverslip, ensuring a clean and transparent surface above. A 3D-printed fiber optic holder was then fixed over the glass coverslip, ensuring that the hole in the fiber optic holder perfectly aligned with the circular glass coverslip. The surrounding area was further secured to the mouse skull with dental cement (Super-Bond C&B, SUN MEDICAL). Last, the scalp around the fiber optic holder was adhered using 3M VetBond tissue adhesive.

### Implantation of neural probes

Following the injection of UCNPs, $WO_{3-x}$, or HUP into anesthetized mice, a 32-channel nickel-titanium microwire array electrode (KD-MWA, KeDouBC) was slowly inserted into the hippocampal region (AP: −2 mm, ML: +1.2 mm, and DV: −1.5 mm). Upon reaching the target area, the electrode was secured to the skull using dental cement (Super-Bond C&B, SUN MEDICAL). The microwire array electrode was then connected to an Intan 128-channel Stimulation/Recording Controller (Intan Technologies) for in vivo electrophysiological recording.

### Induction of epilepsy

Epilepsy was induced in wild-type C57BL/6J mice using the excitotoxin KA. Anesthetized mice received an intraperitoneal injection of KA (15 mg/kg in saline) to induce seizures.

### NIR neurostimulation in the MS for the theta entrainment

All surgeries were performed using a stereotaxic frame from RWD Life Science Co. Ltd. (RWD). Ten-week-old wild-type C57BL/6J mice were anesthetized with isoflurane gas administered via a desktop animal anesthesia machine from RWD. Scalp incisions and craniotomies were performed at the coordinates for MS (AP: +0.9 mm, ML: +0.1 mm, and DV: −4.1 mm) and hippocampus (AP: −2 mm, ML: +1.2 mm, and DV: −1.5 mm). Circular holes approximately 5 mm in diameter were drilled in the skull over the target brain regions. HUP (3.75 μl) was sonicated for 5 min and injected into the MS region (AP: +0.9 mm, ML: +0.1 mm, and DV: −4.1 mm) at a rate of 0.375 μl/min using a microsyringe (Pump 11 Elite, Harvard Apparatus). Following the injection, the needle was left in place for an additional 10 min before being slowly withdrawn. A circular glass coverslip of the same diameter (5 mm) was placed over the hole, with the edges sealed to the skull using either 3M VetBond tissue adhesive or Kwik-Cast silicone sealant. Dental cement (Super-Bond C&B, SUN MEDICAL) was applied to secure the glass coverslip, ensuring a clean and transparent surface above. A 3D-printed fiber optic holder was then fixed over the glass coverslip, ensuring that the hole in the

fiber optic holder perfectly aligned with the circular glass coverslip. The surrounding area was further secured to the mouse skull with dental cement. Last, the scalp around the fiber optic holder was adhered using 3M VetBond tissue adhesive. A 32-channel nickel-titanium microwire array electrode (KD-MWA, KeDouBC) was slowly inserted into the hippocampus. Upon reaching the target region, the electrode was secured to the skull using dental cement. The scalp around the fiber optic holder was adhered with 3M VetBond tissue adhesive.

Seven days following the surgery, the microwire array electrode was connected to an Intan 128-channel Stimulation/Recording Controller (Intan Technologies). The tip of an NIR transmitting optical fiber (200 μm in diameter) was inserted into the fiber optic holder and secured 2 mm above the skull with two screws, targeting the injection site in the MS region. A Python program was used to interface with an external camera for recording. A DAQ card (USB-6009, National Instruments) was used to synchronize the Intan 128-channel Stimulation/Recording Controller (Intan Technologies) with the camera recording and NIR laser (MDL-AF-980-6 W, ED42063). The NIR laser delivered 10-s pulses of 6 to 12 Hz, 15 ms (1.2 W peak power, 11.8 to 23.5 W/cm$^2$) transcranial NIR stimulation. On the same day, epilepsy was induced in mice using KA. After the induction of epilepsy, LFP (sampled at 30 kHz) was acquired as described above and the NIR laser delivered 10-s pulses of 8 Hz, 15 ms (1.2 W peak power, 15.7 W/cm$^2$) transcranial NIR stimulation every 60 s.

### In vivo electrophysiological recording of suppressing seizure by NIR stimulation

Seven days following the nanoparticle injection and microwire array electrode implantation surgery, epilepsy was induced in the mice using KA. After induction, the microwire array electrode was connected to an Intan 128-channel Stimulation/Recording Controller (Intan Technologies). An NIR transmitting optical fiber (200 μm in diameter) was inserted into the fiber optic holder and secured 2 mm above the skull with two screws, targeting the injection site in the MS region.

A Python program was used to interface with an external camera for recording. A data acquisition (DAQ) card (USB-6009, National Instruments) was used to synchronize the Intan 128-channel Stimulation/Recording Controller (Intan Technologies) with the camera recording and NIR laser (MDL-AF-980-6 W, ED42063). The NIR laser delivered up to 60-s pulses of 8 Hz, 15 ms-pulse duration (1.2 W peak power, 15.7 W/cm$^2$) transcranial NIR stimulation.

The recorded brain signals were read using the RHS Reader (Intan) software and saved into a CSV file, capturing voltage and time data. The voltage data were then subjected to short-time Fourier transform (STFT) to obtain the spectrogram, providing a time-frequency representation of the signal. The STFT window size was set to 2048*20 samples to ensure detailed frequency analysis. The resulting spectrogram was plotted using a color mesh, with the $x$ axis representing time and the $y$ axis representing frequency. The intensity of the frequencies was displayed in decibels, and a color bar was included to represent the intensity scale, ensuring clear visualization of the signal's frequency components.

### NIR neurostimulation in the VTA

All surgeries were performed using a stereotaxic frame from RWD Life Science Co. Ltd. (RWD). Eight-week-old wild-type C57BL/6J mice were anesthetized with isoflurane gas administered via a desktop animal anesthesia machine from RWD. A scalp incision and craniotomy were performed at the coordinates for the VTA. A circular hole approximately 5 mm in diameter was drilled in the skull over the target brain region. A 3.75-μl mixture of HUP was sonicated for 5 min and injected into the VTA at a rate of 0.375 μl/min using a microsyringe (Pump 11 Elite, Harvard Apparatus). Following injection, the needle was left in place for an additional 10 min before being slowly withdrawn. A circular glass coverslip of the same diameter (5 mm) was placed over the hole, with the edges sealed to the skull using either 3M VetBond tissue adhesive or Kwik-Cast silicone sealant. Dental cement was applied to secure the glass coverslip, ensuring a clean and transparent surface above. A 3D-printed fiber optic holder was then fixed over the glass coverslip, ensuring that the hole in the fiber optic holder perfectly aligned with the circular glass coverslip. The surrounding area was further secured to the mouse skull with dental cement. Last, the scalp around the fiber optic holder was adhered using 3M VetBond tissue adhesive. The tip of an NIR transmitting optical fiber (200 μm in diameter) was inserted into the fiber optic holder and secured 2 mm above the skull with two screws, targeting the injection site in the VTA.

Seven days post-surgery, the mice were placed in a custom Y-shaped maze for a 10-min preexperiment to allow them to acclimate to the maze environment. Following this acclimation period, the mice entered the 20- to 60-min training phase. For three consecutive days, the mice were placed in the Y-maze, where one of the arms was designated as the light stimulation arm. Upon entering this arm, a programmed light stimulus of a specific frequency was activated. The specific implementation methods are as follows.

Two external cameras were used, with camera 1 used for object detection and camera 2 for video recording. Using Python, frames from camera 1 were captured, and one of the arms of the Y-shaped maze was selected as the ROI.

The ROI was converted to grayscale, and binary thresholding was applied to distinguish the black object from the background. The threshold value used was 30, resulting in an inverted binary image. Contours were extracted from the binary image using cv2.findContours. All detected contours were analyzed, and those with an area greater than 80 were considered as the target mouse.

Upon detection, a DAQ card (USB-6009, National Instruments) was triggered to control the NIR laser (MDL-980) to emit 20 Hz, 15 ms (1.2 W peak power, 39.2 W/cm$^2$) NIR pulses through the skull every 10 s. Specifically, the NIR pulses were emitted for 1 s every 10 s, resulting in 20 pulses per 10-s trial.

After three consecutive days of training, the mice entered the 20–60 min experimental phase. The light stimulation arm was the same as in the training phase, and the mice's recognition and the light stimulation program remained consistent with the training phase.

After the experiment, the video recorded by camera 2 was processed. The ROI was manually selected in the video frames using the same black mouse contour recognition parameters as those used for camera 1 to ensure consistent mouse identification. The video data were processed frame by frame. Each frame was converted to the hue-saturation-value (HSV) color space, and an adjusted HSV threshold was applied to create a mask for the black region. The ROI mask was then applied to isolate the black region within the designated ROI. Contours of the black region were detected, and those within the specified area thresholds were retained. The centroids of the valid contours were calculated and recorded as the positional data of the mouse.

The saved mouse position data file was loaded, and $x$ and $y$ coordinates were extracted from the position data. The Y-maze were divided into discrete grids. The distribution heatmap matrix values

were calculated by normalizing the time spent in each grid to the total time spent in the maze, representing the relative activity frequency. Last, a Gaussian filter was applied to the normalized heatmap for smoothing and highlighting high-frequency activity areas. The final heatmap was generated using the matplotlib library, with colors indicating the relative activity frequency at each position.

### In vivo DA measurement upon NIR neuromodulation

UCNPs (3.75 μl) (5 mg UCNPs dispersed in 50 μl of PBS), $WO_{3-x}$ (5 mg $WO_{3-x}$ dispersed in 50 μl of PBS), or HUP (5 mg UCNPs and 5 mg $WO_{3-x}$ dispersed in 50 μl of PBS) was injected unilaterally into the VTA of 10-week-old C57BL/6J mice. Seven days later, the mice were used for in vivo Amperometric i-t Curve recording of dopamine release. The specific implementation methods are as follows.

Mice were anesthetized with intraperitoneal injection of urethane (1.5 g/kg) dissolved in sterile saline and placed in the stereotaxic frame. A carbon fiber electrode was lowered into the ventral striatum (AP: +1.3 mm, ML: +0.8 mm, and DV: −4.2 mm). One Ag wire (auxiliary electrode) and one Ag/AgCl wire (reference electrode) were inserted into the cortex of the contralateral hemisphere. An optic fiber for NIR light delivery was elevated 2 mm above the VTA cranial window.

Shanghai ChenHua 760E Electrochemical Workstation was used for I-t curve recordings and data acquisition. The initial potential 0.25 V versus Ag/AgCl reference was applied to the carbon fiber electrode, and the sample interval was 0.1 s.

To assess the ability of transcranial application of NIR light to elicit dopamine release, NIR irradiation (15 ms pulses at 20 Hz, 1.2 W peak power, and 39.2 W/cm$^2$) was applied during I-t recording. All recording sessions were 40 s, with stimulation applied from 10 to 20 s since session started (total 10 s on).

### NIR neurostimulation in the M2

This study involved an experimental group of mice that received injections of 3 μl of 200 mg/ml HUP in the secondary motor cortex (M2) (AP: +1 mm, ML: +0.78 mm, and DV: −1 mm), as well as control groups of mice injected with PBS. All animals were allowed to fully recover for 24 hours after the stereotaxic injection, during which they exhibited normal behavior before behavioral experiments commenced. Subsequent behavioral testing was performed on day 1 postinjection for recovery. The fiber optic holder on the mouse's head is green, allowing a custom Python program to track the mouse's movement trajectory. The fiber optic is inserted into the light fixture to ensure that it is perpendicular to the mouse's head. In each experiment, a mouse is placed in a 20 cm by 20 cm white box, allowing it to explore freely. A Canon Rebel T6 camera records videos of the mouse at a resolution of 640 pixels by 480 pixels and 30 frames per second for 10 s before, 10 s during, and 10 s after NIR photostimulation. Before the light stimulation, the mice are placed in the box for at least 20 min in advance to allow for habituation. NIR photostimulation is initiated when the mouse remains stationary for at least 10 s. During NIR photostimulation, a 980-nm laser is emitted in pulsed mode from the fiber tip, with a frequency of 4 Hz and a pulse width of 150 ms. The laser illuminates the mouse's M2 region at power levels of 1.2 W peak value for a duration of 10 s.

### Evaluation of NIR heating effect in mouse brain

C57BL/6J mice were anesthetized under 0.5% isoflurane inhalation and placed in the stereotaxic platform. An optical fiber (200 μm in diameter) was positioned 2 mm above the skull, targeting the brain ROI, to deliver the NIR pulses. We used an ultrafine sheathed thermocouple sensor (RKL-QB-K-2 × 0.1, RUIKELI) connected to a K-type thermocouple thermometer (YET-620 L, RUIKELI) to measure the temperature. The sensor was either inserted into the target deep brain region or placed on the cortex surface to measure local temperatures in anesthetized mice. The temperature changes for the four NIR irradiation protocols used in this study are summarized in fig. S23 and table S1.

### Histology

C57BL/6J mice were anesthetized and transcardially perfused with 1× PBS, followed by 4% PFA in PBS. For imaging c-Fos in the MS and VTA (Figs. 5 and 7), transcardial perfusion was performed at 90 min after the animals of different experimental and control groups received NIR illumination. Brains were dissected, postfixed for 48 hours at 4°C in 4% PFA to ensure adequate fixation. Afterward, the brains were dehydrated, embedded in wax, and followed by cooling at −20°C on a freezing stage until the wax was completely solidified. Coronal sections (5-μm–thick) were collected on a cryostat (RM2016; Leica). The brain slices were then deparaffinized, rehydrated, and subjected to antigen retrieval in sodium citrate buffer (pH 6.0) at a sub-boiling temperature. After blocking with 3% BSA for 30 min at room temperature, the slices were incubated with the primary antibody overnight at 4°C. The antibody for c-Fos, GFAP, and Iba-1 is ab208942 (Abcam), (E4L7M) XP Rabbit mAb #80788, and ab178846 (Abcam), respectively. Following this, the slices were washed three times with 1× PBS and incubated with the corresponding secondary antibodies for 50 min at room temperature in darkness. After three 1× PBS washes, the slices were incubated with DAPI solution for 10 min at room temperature in the dark. Fluorescent imaging was performed using a digital slide scanner (Pannoramic MIDI; 3DHISTECH). For statistics, slices from at least three animals were obtained, imaged, and analyzed. All imaging and analyses were performed blind to the experimental conditions.

### Theoretical calculation of photocurrent generated by HUP via 980-nm laser excitation

We estimate the photocurrent generated by HUP when exposed to a 1-W 980-nm laser with a spot size of 1 mm$^2$, assuming a pulse duration of 1 s. To measure the photocurrent, we dropcast HUP onto an FTO electrode. Considering the 15-mm water layer between the glass sidewall and the FTO electrode, and an attenuation coefficient of water at 980 nm of approximately 0.4 mm$^{-1}$, the power at the FTO is reduced to about

$$I_{\mathrm{FTO}} = 1 \times \exp(-1 \times 15 \times 0.4) = 0.0025\ \mathrm{W} \tag{3}$$

The upconversion efficiency is approximately 1.4%, which leads to

$$I_{\mathrm{blue}} = 0.0025 \times 1.4\,\% = 3.5 \times 10^{-5}\ \mathrm{W} \tag{4}$$

Given that the wavelength is around 450 nm, each photon has an energy of

$$h\nu = 6.6 \times 10^{-34} \times \left( \frac{3 \times 10^{8}}{450 \times 10^{-9}} \right) = 4.4 \times 10^{-19}\ \mathrm{J} \tag{5}$$

This results in approximately $8 \times 10^{13}$ photons/s, calculated as

$$\frac{3.5 \times 10^{-5}}{4.4 \times 10^{-19}} = 8 \times 10^{13}\ \text{photons/s} \tag{6}$$

With the Internal Photoelectric Conversion Efficiency of $WO_{3-x}$ at around 5% for 450 nm, about $4 \times 10^{12}$ electrons are excited per second

$$8 \times 10^{13} \times 5\% = 4 \times 10^{12} \text{ electrons/s} \quad (7)$$

Since each electron carries a charge of $1.6 \times 10^{-19}$ C, the photocurrent is

$$1.6 \times 10^{-19} \times 4 \times 10^{12} = 6.4 \times 10^{-7} \frac{\text{C}}{\text{s}} \approx 0.64\ \mu\text{A} \quad (8)$$

We note that this theoretical calculation agrees with our experimental results very well.

Further considering the spot size of 0.01 $cm^2$, the photocurrent density is

$$\frac{0.64}{0.01} = 64\ \frac{\mu\text{A}}{\text{cm}^2} \quad (9)$$

Regarding the brain ROIs, MS and VTA, which are approximately 4 mm beneath the skull, the light power at this depth is

$$I = 1 \times \exp(-1 \times 4 \times 0.6) = 0.09\ \text{W} \quad (10)$$

which is 36 times than the light intensity at the FTO electrode. Consequently, we estimate that the photocurrent density in the deep brain regions is on the order of microampere per square centimeter, well above the threshold required to activate neurons.

### Statistical analysis

The variances in cell density and population percentage (Figs. 5 and 7), raw and normalized neural firing rate, cumulative DA release (Fig. 6) and place preference (Fig. 6) for brain slices, electrophysiological traces, amperometric i-t curves, or behavioral trials were calculated. For statistics, data were analyzed using Graph Prism 8 (v.8.3.0, GraphPad Software), PyCharm (2022.1.3) and MATLAB (R2023b). For microscopy, images were analyzed using ImageJ (win64, v.1.54; National Institutes of Health). Our study investigates a single factor—HUP-mediated NIR stimulation—with two levels: animals receiving complete HUP + NIR versus animals lacking at least one component of the HUP + NIR system. Therefore, a one-way analysis of variance (ANOVA) test was used to quantify differences between the positive group (complete HUP + NIR) and any control groups (lacking at least one component of the system). No statistical methods were used to predetermine sample sizes, but group sizes for immunohistochemistry and behavioral tests are similar to previously published studies exploring nanoparticle mediated neuromodulation. All datasets used for one-way ANOVA tests passed the Shapiro-Wilk normality test performed in MATLAB. Tukey's post hoc comparison test was applied to identify significant differences between groups following one-way ANOVA test. $P < 0.05$ was considered statistically significant. Analysis was performed in a manner blinded to treatment assignments in all behavioral experiments, immunofluorescence imaging, and quantification. No neurons or survival animals from surgeries were excluded from analysis.

## Supplementary Materials

**The PDF file includes:**

Figs. S1 to S23
Table S1
Legend for data S1

**Other Supplementary Material for this manuscript includes the following:**

Data S1

## REFERENCES AND NOTES


1. H. Knotkova, C. Hamani, E. Sivanesan, M. F. E. Le Beuffe, J. Y. Moon, S. P. Cohen, M. A. Huntoon, Neuromodulation for chronic pain. *Lancet* **397**, 2111–2124 (2021).
2. K. Famm, B. Litt, K. J. Tracey, E. S. Boyden, M. Slaoui, Drug discovery: A jump-start for electroceuticals. *Nature* **496**, 159–161 (2013).
3. A. M. Lozano, N. Lipsman, H. Bergman, P. Brown, S. Chabardes, J. W. Chang, K. Matthews, C. C. McIntyre, T. E. Schlaepfer, M. Schulder, Y. Temel, J. Volkmann, J. K. Krauss, Deep brain stimulation: Current challenges and future directions. *Nat. Rev. Neurol.* **15**, 148–160 (2019).
4. K. Servick, Deep brain stimulation takes new aim at depression. *Science* **374**, 1182–1183 (2021).
5. M. Creed, V. J. Pascoli, C. Lüscher, Refining deep brain stimulation to emulate optogenetic treatment of synaptic pathology. *Science* **347**, 659–664 (2015).
6. O. Karatum, M. J. Gwak, J. Hyun, A. Onal, G. R. Koirala, T. I. Kim, S. Nizamoglu, Optical neuromodulation at all scales: From nanomaterials to wireless optoelectronics and integrated systems. *Chem. Soc. Rev.* **52**, 3326–3352 (2023).
7. S. Jiang, X. Wu, N. J. Rommelfanger, Z. Ou, G. Hong, Shedding light on neurons: Optical approaches for neuromodulation. *Natl. Sci. Rev.* **9**, nwac007 (2022).
8. A. Fernandez-Ruiz, A. Oliva, H. Chang, High-resolution optogenetics in space and time. *Trends Neurosci.* **45**, 854–864 (2022).
9. A. J. Taal, I. Uguz, S. Hillebrandt, C.-K. Moon, V. Andino-Pavlovsky, J. Choi, C. Keum, K. Deisseroth, M. C. Gather, K. L. Shepard, Optogenetic stimulation probes with single-neuron resolution based on organic LEDs monolithically integrated on CMOS. *Nat. Electron.* **6**, 669–679 (2023).
10. S. Chen, A. Z. Weitemier, X. Zeng, L. He, X. Wang, Y. Tao, A. J. Y. Huang, Y. Hashimotodani, M. Kano, H. Iwasaki, L. K. Parajuli, S. Okabe, D. B. L. Teh, A. H. All, I. Tsutsui-Kimura, K. F. Tanaka, X. Liu, T. J. McHugh, Near-infrared deep brain stimulation via upconversion nanoparticle-mediated optogenetics. *Science* **359**, 679–684 (2018).
11. J. A. Sahel, E. Boulanger-Scemama, C. Pagot, A. Arleo, F. Galluppi, J. N. Martel, S. D. Esposti, A. Delaux, J. B. de Saint Aubert, C. de Montleau, E. Gutman, I. Audo, J. Duebel, S. Picaud, D. Dalkara, L. Blouin, M. Taiel, B. Roska, Partial recovery of visual function in a blind patient after optogenetic therapy. *Nat. Med.* **27**, 1223–1229 (2021).
12. X. Wu, F. Yang, S. Cai, K. Pu, G. Hong, Nanotransducer-enabled deep-brain neuromodulation with NIR-II light. *ACS Nano* **17**, 7941–7952 (2023).
13. K. Inoue, M. del Carmen Marín, S. Tomida, R. Nakamura, Y. Nakajima, M. Olivucci, H. Kandori, Red-shifting mutation of light-driven sodium-pump rhodopsin. *Nat. Commun.* **10**, 1993 (2019).
14. C. Chen, F. Wang, S. Wen, Q. P. Su, M. C. L. Wu, Y. Liu, B. Wang, D. Li, X. Shan, M. Kianinia, I. Aharonovich, M. Toth, S. P. Jackson, P. Xi, D. Jin, Multi-photon near-infrared emission saturation nanoscopy using upconversion nanoparticles. *Nat. Commun.* **9**, 3290 (2018).
15. X. Liu, H. Chen, Y. Wang, Y. Si, H. Zhang, X. Li, Z. Zhang, B. Yan, S. Jiang, F. Wang, S. Weng, W. Xu, D. Zhao, J. Zhang, F. Zhang, Near-infrared manipulation of multiple neuronal populations via trichromatic upconversion. *Nat. Commun.* **12**, 5662 (2021).
16. F. Sun, H. Shen, Q. Yang, Z. Yuan, Y. Chen, W. Guo, Y. Wang, L. Yang, Z. Bai, Q. Liu, M. Jiang, J. W. Y. Lam, J. Sun, R. Ye, R. T. K. Kwok, B. Z. Tang, Dual behavior regulation: Tether-free deep-brain stimulation by photothermal and upconversion hybrid nanoparticles. *Adv. Mater.* **35**, 2210018 (2023).
17. Y. Li, B. Yang, Y. Wang, Z. Huang, J. Wang, X. Pu, J. Wen, Q. Ao, K. Xiao, J. Wu, G. Yin, Postoperatively noninvasive optogenetic stimulation via upconversion nanoparticles enhancing sciatic nerve repair. *Nano Lett.* **24**, 5403–5412 (2024).
18. X. Wu, Y. Jiang, N. J. Rommelfanger, F. Yang, Q. Zhou, R. Yin, J. Liu, S. Cai, W. Ren, A. Shin, K. S. Ong, K. Pu, G. Hong, Tether-free photothermal deep-brain stimulation in freely behaving mice via wide-field illumination in the near-infrared-II window. *Nat. Biomed. Eng.* **6**, 754–770 (2022).
19. D. Nelidova, R. K. Morikawa, C. S. Cowan, Z. Raics, D. Goldblum, H. P. N. Scholl, T. Szikra, A. Szabo, D. Hillier, B. Roska, Restoring light sensitivity using tunable near-infrared sensors. *Science* **368**, 1108–1113 (2020).
20. W. Gao, Y. Sun, M. Cai, Y. Zhao, W. Cao, Z. Liu, G. Cui, B. Tang, Copper sulfide nanoparticles as a photothermal switch for TRPV1 signaling to attenuate atherosclerosis. *Nat. Commun.* **9**, 231 (2018).
21. S. Yoo, S. Hong, Y. Choi, J.-H. Park, Y. Nam, Photothermal inhibition of neural activity with near-infrared-sensitive nanotransducers. *ACS Nano* **8**, 8040–8049 (2014).
22. P. Gupta, R. Chandak, A. Debnath, M. Traner, B. M. Watson, H. Huang, H. G. Derami, H. Baldi, S. Chakrabartty, B. Raman, S. Singamaneni, Augmenting insect olfaction performance through nano-neuromodulation. *Nat. Nanotechnol.* **19**, 677–687 (2024).
23. Y. Zhang, D. Yang, J. Nie, J. Dai, H. Wu, J. C. Zheng, F. Zhang, Y. Fang, Transcranial nongenetic neuromodulation via bioinspired vesicle-enabled precise NIR-II optical stimulation. *Adv. Mater.* **35**, 2208601 (2023).
24. W. Tian, Q. Jia, J. Lin, J. Luo, D. He, J. Yang, T. Guo, H. Guo, Y. Guo, W. Zhang, Remote neurostimulation through an endogenous ion channel using a near-infrared light–activatable nanoagonist. *Sci. Adv.* **10**, eadn0367 (2024).

25. Y. Jiang, Y. Huang, X. Luo, J. Wu, H. Zong, L. Shi, R. Cheng, Y. Zhu, S. Jiang, L. Lan, X. Jia, J. Mei, H. Y. Man, J. X. Cheng, C. Yang, Neural stimulation in vitro and in vivo by photoacoustic nanotransducers. *Matter* **4**, 654–674 (2021).
26. Z. Du, G. Chen, Y. Li, N. Zheng, J.-X. Cheng, C. Yang, Photoacoustic: A versatile nongenetic method for high-precision neuromodulation. *Acc. Chem. Res.* **57**, 1595–1607 (2024).
27. R. Airan, Neuromodulation with nanoparticles. *Science* **357**, 465–465 (2017).
28. M. L. DiFrancesco, F. Lodola, E. Colombo, L. Maragliano, M. Bramini, G. M. Paterno, P. Baldelli, M. D. Serra, L. Lunelli, M. Marchioretto, G. Grasselli, S. Cimò, L. Colella, D. Fazzi, F. Ortica, V. Vurro, C. G. Eleftheriou, D. Shmal, J. F. Maya-Vetencourt, C. Bertarelli, G. Lanzani, F. Benfenati, Neuronal firing modulation by a membrane-targeted photoswitch. *Nat. Nanotechnol.* **15**, 296–306 (2020).
29. H. Su, Z. Liu, Y. Liu, V. P.-Y. Ma, A. Blanchard, J. Zhao, K. Galior, R. B. Dyer, K. Salaita, Light-responsive polymer particles as force clamps for the mechanical unfolding of target molecules. *Nano Lett.* **18**, 2630–2636 (2018).
30. Y. Jiang, R. Parameswaran, X. Li, J. L. Carvalho-de-Souza, X. Gao, L. Meng, F. Bezanilla, G. M. G. Shepherd, B. Tian, Nongenetic optical neuromodulation with silicon-based materials. *Nat. Protoc.* **14**, 1339–1376 (2019).
31. C. Yang, Z. Cheng, P. Li, B. Tian, Exploring present and future directions in nano-enhanced optoelectronic neuromodulation. *Acc. Chem. Res.* **57**, 1398–1410 (2024).
32. H. Cui, S. Zhao, G. Hong, Wireless deep-brain neuromodulation using photovoltaics in the second near-infrared spectrum. *Device* **1**, 100113 (2023).
33. D. I. Medagoda, D. Ghezzi, Organic semiconductors for light-mediated neuromodulation. *Commun. Mater.* **2**, 111 (2021).
34. Z. Wang, C. Tan, M. Peng, Y. Yu, F. Zhong, P. Wang, T. He, Y. Wang, Z. Zhang, R. Xie, F. Wang, S. He, P. Zhou, W. Hu, Giant infrared bulk photovoltaic effect in tellurene for broad-spectrum neuromodulation. *Light Sci. Appl.* **13**, 277 (2024).
35. M. Berggren, E. D. Głowacki, D. T. Simon, E. Stavrinidou, K. Tybrandt, In vivo organic bioelectronics for neuromodulation. *Chem. Rev.* **122**, 4826–4846 (2022).
36. R. Parameswaran, J. L. Carvalho-de-Souza, Y. Jiang, M. J. Burke, J. F. Zimmerman, K. Koehler, A. W. Philips, J. Yi, E. Adams, F. Bezanilla, B. Tian, Photoelectrochemical modulation of neuronal activity with free-standing coaxial silicon nanowires. *Biophys. J.* **114**, 393a (2018).
37. D. Wang, X. Liu, Y. Kang, X. Wang, Y. Wu, S. Fang, H. Yu, M. H. Memon, H. Zhang, W. Hu, Z. Mi, L. Fu, H. Sun, S. Long, Bidirectional photocurrent in p–n heterojunction nanowires. *Nat. Electron.* **4**, 645–652 (2021).
38. P. Li, J. Zhang, H. Hayashi, J. Yue, W. Li, C. Yang, C. Sun, J. Shi, J. Huberman-Shlaes, N. Hibino, B. Tian, Monolithic silicon for high spatiotemporal translational photostimulation. *Nature* **626**, 990–998 (2024).
39. P. Sun, C. Li, C. Yang, M. Sun, H. Hou, Y. Guan, J. Chen, S. Liu, K. Chen, Y. Ma, Y. Huang, X. Li, H. Wang, L. Wang, S. Chen, H. Cheng, W. Xiong, X. Sheng, M. Zhang, J. Peng, S. Wang, Y. Wang, L. Yin, A biodegradable and flexible neural interface for transdermal optoelectronic modulation and regeneration of peripheral nerves. *Nat. Commun.* **15**, 4721 (2024).
40. Y. Jiang, X. Li, B. Liu, J. Yi, Y. Fang, F. Shi, X. Gao, E. Sudzilovsky, R. Parameswaran, K. Koehler, V. Nair, J. Yue, K. H. Guo, Y. Fang, H. M. Tsai, G. Freyermuth, R. C. S. Wong, C. M. Kao, C. T. Chen, A. W. Nicholls, X. Wu, G. M. G. Shepherd, B. Tian, Rational design of silicon structures for optically controlled multiscale biointerfaces. *Nat. Biomed. Eng.* **2**, 508–521 (2018).
41. Y. Huang, Y. Cui, H. Deng, J. Wang, R. Hong, S. Hu, H. Hou, Y. Dong, H. Wang, J. Chen, L. Li, Y. Xie, P. Sun, X. Fu, L. Yin, W. Xiong, S. H. Shi, M. Luo, S. Wang, X. Li, X. Sheng, Bioresorbable thin-film silicon diodes for the optoelectronic excitation and inhibition of neural activities. *Nat. Biomed. Eng.* **7**, 486–498 (2023).
42. A. Prominski, J. Shi, P. Li, J. Yue, Y. Lin, J. Park, B. Tian, M. Y. Rotenberg, Porosity-based heterojunctions enable leadless optoelectronic modulation of tissues. *Nat. Mater.* **21**, 647–655 (2022).
43. J. Tang, N. Qin, Y. Chong, Y. Diao, Yiliguma, Z. Wang, T. Xue, M. Jiang, J. Zhang, G. Zheng, Nanowire arrays restore vision in blind mice. *Nat. Commun.* **9**, 786 (2018).
44. R. Yang, P. Zhao, L. Wang, C. Feng, C. Peng, Z. Wang, Y. Zhang, M. Shen, K. Shi, S. Weng, C. Dong, F. Zeng, T. Zhang, X. Chen, S. Wang, Y. Wang, Y. Luo, Q. Chen, Y. Chen, C. Jiang, S. Jia, Z. Yu, J. Liu, F. Wang, S. Jiang, W. Xu, L. Li, G. Wang, X. Mo, G. Zheng, A. Chen, X. Zhou, C. Jiang, Y. Yuan, B. Yan, J. Zhang, Assessment of visual function in blind mice and monkeys with subretinally implanted nanowire arrays as artificial photoreceptors. *Nat. Biomed. Eng.* **8**, 1018–1039 (2023).
45. M. Jakešová, M. Silverå Ejneby, V. Đerek, T. Schmidt, M. Gryszel, J. Brask, R. Schindl, D. T. Simon, M. Berggren, F. Elinder, E. D. Głowacki, Optoelectronic control of single cells using organic photocapacitors. *Sci. Adv.* **5**, eaav5265 (2019).
46. M. Silverå Ejneby, M. Jakešová, J. J. Ferrero, L. Migliaccio, I. Sahalianov, Z. Zhao, M. Berggren, D. Khodagholy, V. Đerek, J. N. Gelinas, E. D. Głowacki, Chronic electrical stimulation of peripheral nerves via deep-red light transduced by an implanted organic photocapacitor. *Nat. Biomed. Eng.* **6**, 741–753 (2022).
47. D. Rand, M. Jakešová, G. Lubin, I. Vėbraitė, M. David-Pur, V. Đerek, T. Cramer, N. S. Sariciftci, Y. Hanein, E. D. Głowacki, Direct electrical neurostimulation with organic pigment photocapacitors. *Adv. Mater.* **30**, 1707292 (2018).
48. M. Duan, C. Hu, H. Li, Y. Chen, R. Chen, W. Gong, Z. Lu, N. Zhang, R. Long, L. Song, Y. Xiong, Synergizing inter and intraband transitions in defective tungsten oxide for efficient photocatalytic alcohol dehydration to alkenes. *JACS Au* **2**, 1160–1168 (2022).
49. G. Xi, S. Ouyang, P. Li, J. Ye, Q. Ma, N. Su, H. Bai, C. Wang, Ultrathin W18O49 nanowires with diameters below 1 nm: Synthesis, near-infrared absorption, photoluminescence, and photochemical reduction of carbon dioxide. *Angew. Chem. Int. Ed. Engl.* **51**, 2395–2399 (2012).
50. Y. Liu, Y. Lu, X. Yang, X. Zheng, S. Wen, F. Wang, X. Vidal, J. Zhao, D. Liu, Z. Zhou, C. Ma, J. Zhou, J. A. Piper, P. Xi, D. Jin, Amplified stimulated emission in upconversion nanoparticles for super-resolution nanoscopy. *Nature* **543**, 229–233 (2017).
51. I. Grigioni, M. Abdellah, A. Corti, M. V. Dozzi, L. Hammarstrom, E. Selli, Photoinduced charge-transfer dynamics in $WO_3$/$BiVO_4$ photoanodes probed through midinfrared transient absorption spectroscopy. *J. Am. Chem. Soc.* **140**, 14042–14045 (2018).
52. Y. Sun, W. Feng, P. Yang, C. Huang, F. Li, The biosafety of lanthanide upconversion nanomaterials. *Chem. Soc. Rev.* **44**, 1509–1525 (2015).
53. X. F. Liu, J. R. Qiu, Recent advances in energy transfer in bulk and nanoscale luminescent materials: From spectroscopy to applications. *Chem. Soc. Rev.* **44**, 8714–8746 (2015).
54. S. V. G. H. V. Demir, *Applied Nanophotonics* (Cambridge Univ. Press, ed. 1, 2019).
55. X. D. Yang, F. Li, W. Liu, L. Chen, J. J. Qi, W. L. Sun, F. Pan, T. Duan, F. B. Sun, Oxygen vacancy-induced spin polarization of tungsten oxide nanowires for efficient photocatalytic reduction and immobilization of uranium(VI) under simulated solar light. *Appl. Catal. B* **324**, 122202 (2023).
56. C. Feng, X. H. Mi, D. W. Zhong, W. M. Zhang, Y. P. Liu, D. Y. Fan, M. Li, J. F. Hai, Z. H. Lu, Chemically bonded N-PDI-P/WO organic-inorganic heterojunction with improved photoelectrochemical performance. *Catalysts* **10**, 122 (2020).
57. C. K. Kim, A. Adhikari, K. Deisseroth, Integration of optogenetics with complementary methodologies in systems neuroscience. *Nat. Rev. Neurosci.* **18**, 222–235 (2017).
58. V. A. Lórenz-Fonfría, J. Heberle, Channelrhodopsin unchained: Structure and mechanism of a light-gated cation channel. *Biochim. Biophys. Acta* **1837**, 626–642 (2014).
59. T. Mager, D. Lopez de la Morena, V. Senn, J. Schlotte, A. D. Errico, K. Feldbauer, C. Wrobel, S. Jung, K. Bodensiek, V. Rankovic, L. Browne, A. Huet, J. Jüttner, P. G. Wood, J. J. Letzkus, T. Moser, E. Bamberg, High frequency neural spiking and auditory signaling by ultrafast red-shifted optogenetics. *Nat. Commun.* **9**, 1750 (2018).
60. R. L. D. a. M. E. G. L. Laurence M. Peter, P. Sudhagar, N. Roy, R. Vedarajan, A. Devadoss, C. Terashima, K. Nakata, A. Fujishima, *Photoelectrochemical Solar Fuel Production: From Basic Principles to Advanced Devices* (Springer, 2016).
61. J. J. Shi, Y. M. Li, Y. S. Li, D. M. Li, Y. H. Luo, H. J. Wu, Q. B. Meng, From ultrafast to ultraslow: Charge-carrier dynamics of perovskite solar cells. *Joule* **2**, 879–901 (2018).
62. O. K. Coskun, M. Muñoz, S. Dongare, W. Dean, B. E. Gurkan, Understanding the electrode-electrolyte interfaces of ionic liquids and deep eutectic solvents. *Langmuir* **40**, 3283–3300 (2024).
63. Y. Wang, Y. Shen, X. Cai, J. Yu, C. Chen, B. Tan, N. Tan, H. Cheng, X. Fan, X. Wu, J. Liu, S. Wang, Y. Wang, Z. Chen, Deep brain stimulation in the medial septum attenuates temporal lobe epilepsy via entrainment of hippocampal theta rhythm. *CNS Neurosci. Ther.* **27**, 577–586 (2021).
64. R. Lycke, R. Kim, P. Zolotavin, J. Montes, Y. C. Sun, A. Koszeghy, E. Altun, B. Noble, R. K. Yin, F. He, N. Totah, C. Xie, L. Luan, Low-threshold, high-resolution, chronically stable intracortical microstimulation by ultraflexible electrodes. *Cell Rep.* **42**, 112554 (2023).
65. Y. Y. Dong, Y. F. Li, X. K. Xiang, Z. C. Xiao, J. Hu, Y. L. Li, H. H. Li, H. L. Hu, Stress relief as a natural resilience mechanism against depression-like behaviors. *Neuron* **111**, 3789–3801. e6 (2023).
66. A. K. Friedman, J. J. Walsh, B. Juarez, S. M. Ku, D. Chaudhury, J. Wang, X. Li, D. M. Dietz, N. Pan, V. F. Vialou, R. L. Neve, Z. Yue, M. H. Han, Enhancing depression mechanisms in midbrain dopamine neurons achieves homeostatic resilience. *Science* **344**, 313–319 (2014).
67. L. Willmore, C. Cameron, J. Yang, I. B. Witten, A. L. Falkner, Behavioural and dopaminergic signatures of resilience. *Nature* **611**, 124–132 (2022).
68. D. Chaudhury, J. J. Walsh, A. K. Friedman, B. Juarez, S. M. Ku, J. W. Koo, D. Ferguson, H.-C. Tsai, L. Pomeranz, D. J. Christoffel, A. R. Nectow, M. Ekstrand, A. Domingos, M. S. Mazei-Robison, E. Mouzon, M. K. Lobo, R. L. Neve, J. M. Friedman, S. J. Russo, K. Deisseroth, E. J. Nestler, M.-H. Han, Rapid regulation of depression-related behaviours by control of midbrain dopamine neurons. *Nature* **493**, 532–536 (2013).
69. K. M. Tye, J. J. Mirzabekov, M. R. Warden, E. A. Ferenczi, H.-C. Tsai, J. Finkelstein, S.-Y. Kim, A. Adhikari, K. R. Thompson, A. S. Andalman, L. A. Gunaydin, I. B. Witten, K. Deisseroth, Dopamine neurons modulate neural encoding and expression of depression-related behaviour. *Nature* **493**, 537–541 (2013).
70. T. C. Weidner, D. Vincenz, M. Brocka, J. Tegtmeier, A. M. Oelschlegel, F. W. Ohl, J. Goldschmidt, M. T. Lippert, Matching stimulation paradigms resolve apparent differences between optogenetic and electrical VTA stimulation. *Brain Stimul.* **13**, 363–371 (2020).
71. S. F. Owen, M. H. Liu, A. C. Kreitzer, Thermal constraints on in vivo optogenetic manipulations. *Nat. Neurosci.* **22**, 1061–1065 (2019).

72. K. Y. Kwan, A. J. Allchorne, M. A. Vollrath, A. P. Christensen, D.-S. Zhang, C. J. Woolf, D. P. Corey, TRPA1 contributes to cold, mechanical, and chemical nociception but is not essential for hair-cell transduction. *Neuron* **50**, 277–289 (2006).
73. L. L. Cai, C. Y. Yang, W. F. Jia, Y. W. Liu, R. Xie, T. Lei, Z. H. Yang, X. Q. He, R. S. Tong, H. L. Gao, Endo/lysosome-escapable delivery depot for improving BBB transcytosis and neuron targeted therapy of Alzheimer's disease. *Adv. Funct. Mater.* **30**, 1909999 (2020).
74. Y. X. Liu, S. B. Cheng, S. P. Zhan, X. F. Wu, Manipulating energy transfer in UCNPs@SiO@Ag nanoparticles for efficient infrared photocatalysis. *Inorg. Chem.* **60**, 5704–5710 (2021).
75. R. Chen, G. Romero, M. G. Christiansen, A. Mohr, P. Anikeeva, Wireless magnetothermal deep brain stimulation. *Science* **347**, 1477–1480 (2015).
76. S. Rao, R. Chen, A. A. LaRocca, M. G. Christiansen, A. W. Senko, C. H. Shi, P. H. Chiang, G. Varnavides, J. Xue, Y. Zhou, S. Park, R. Ding, J. Moon, G. Feng, P. Anikeeva, Remotely controlled chemomagnetic modulation of targeted neural circuits. *Nat. Nanotechnol.* **14**, 967–973 (2019).
77. S. Zha, H. Liu, H. Li, H. Li, K. L. Wong, A. H. All, Functionalized nanomaterials capable of crossing the blood-brain barrier. *ACS Nano* **18**, 1820–1845 (2024).

**Acknowledgments:** We thank Y. Gao (University of Science and Technology of China), X. Li (Nanjing Normal University), and Z. Wang (Shanghai Institute of Microsystem and Information Technology) for the helpful discussion in the mechanism of photocurrent generation of $WO_{3-x}$. We also thank F. He and F. Li (Shanghai Institute of Optics and Fine Mechanics) for helpful discussion and guidance in two-photon microscopy imaging. **Funding:** This work was supported by National Key R & D Program of China grant 2021ZD0201600 (L.S.), Young Scientists Fund of the National Natural Science Foundation of China grant 62305368 (L.S.), Shanghai Municipal Science and Technology Major Project grant 2021SHZDZX (L.S.), CAS Pioneer Hundred Talents program (L.S. and P.T.), CAS Young Talents Training Program (L.S., P.T., and K.Z.), National Science Fund for Excellent Young Scholars (K.Z.), National Natural Science Foundation of China grant 12174031 (J.S.). **Author contributions:** Conceptualization: L.S. Project administration: L.S. Funding acquisition: L.S., P.T., K.Z., JS., and Y. Ye. Methodology: L.S., P.T., and S.J. Synthesis of nanoparticles: C.M. and L.G. Optical measurements: L.J., M.N., and S.J. Photocurrent measurements: S.J., L.G., and Y.Z. Two-photon fluorescence imaging: S.J. Electron imaging: L.J. Patch-clamp experiment: S.J., Y. Yuan, B.L., and M.C. In vitro and in vivo experiments: S.J., J.L., and L.J. Data analysis: L.S., P.T., S.J., Y. Ye, G.L., Y. Yang, Y.T., H.S., and K.Z. Visualization: S.J. Writing—original draft: L.S. and S.J. Writing—review and editing: K.Z., P.T., and S.J. All authors discussed the results and commented on the manuscript at all stages. **Competing interests:** The authors have a patent application related to this work. The current patent status has entered substantive examination phase. The patent granting organization is China National Intellectual Property Administration (CNIPA). The patent authors are L.S., J.L., S.J., and L.G. The patent number is 02411383608.7, and the patent application date is 30 September 2024. The authors declare that they have no other competing interests. **Data and materials availability:** All data needed to evaluate the conclusions in the paper are present in the paper and/or the Supplementary Materials. The original code has been deposited at Zenodo (https://doi.org/10.5281/zenodo.14729162).

Submitted 2 October 2024
Accepted 12 May 2025
Published 13 June 2025
10.1126/sciadv.adt4771